A framework for formulating and implementing non-associative plasticity models for shell buckling computations

A framework for formulating and implementing non-associative plasticity models for shell buckling computations

Apostolos Nasikas*, Spyros A. Karamanos◆[1] and Stefanos-Aldo Papanicolopulos*

* Institute for Infrastructure and Environment, School of Engineering,
The University of Edinburgh, Scotland, UK

◆ Department of Mechanical Engineering,
University of Thessaly, Volos, Greece

Abstract

In modelling the behavior of thick-walled metal shells under compressive loads, the use of J_2 flow theory can lead to unrealistic buckling estimates, while alternative 'corner' models, despite offering good predictions, have not been widely adopted for structural computations due to their complexity. The present work develops a new and efficient plasticity model for predicting the structural response of compressed metal shells. It combines the simplicity of the Von Mises yield surface, with a non-associative flow rule, mimicking the effect of a yield surface corner. This allows for tracing the equilibrium path of the loaded shell and identifying consistently structural instability, employing a single constitutive model. A robust backward-Euler integration scheme, suitable for both three-dimensional (solid) and shell elements is developed, along with the corresponding consistent algorithmic moduli for nonlinear isotropic hardening materials, accounting rigorously for the nonlinear dependence of plastic straining on the direction of strain increments. The model is implemented in ABAQUS as a user material subroutine. Simulations of thick-walled metal cylinders under compression predict structural instability in good agreement with experimental data.

[1] Corresponding author. Tel +30 24210 74086; fax: +30 24210 74012
e-mail address: skara@mie.uth.gr (S. A. Karamanos)

Keywords:

Non-Associative Plasticity; Pseudo-Corner Theory; Shell Buckling; Structural Instability; Finite Element Analysis; Metal Shell Strength; Computational Plasticity

1 Introduction

Inelastic constitutive models based on associative plasticity can accurately simulate metal material behavior and are suitable for general-purpose analysis of metal components and structures. However, in problems of strain localization and plastic buckling, which occur well into the inelastic range of the material, the use of the J_2 flow theory (J2FT) often results in bifurcation load predictions significantly higher than those observed experimentally. On the other hand, approaches that use the J_2 deformation theory (J2DT) provide estimates more consistent with the experimental data e.g. (Batdorf, 1949; Gerard & Becker, 1957).

In structural instability problems, it is quite difficult to identify accurately the onset of bifurcation, mainly because of its tangential (non-abrupt) character (Kyriakides & Corona, 2007). Furthermore, end support effects and, most importantly, the presence of small inevitable geometric imperfections do not allow for clear interpretation of experimental buckling results. In this perspective, the introduction of imperfections in modelling using J2FT may suffice to predict maximum buckling loads observed in buckling experiments e.g. (Shamass et al., 2014). Nonetheless, to obtain good predictions in terms of bucking load and, more markedly, in terms of the corresponding deformation, the necessary imperfection amplitudes can become unrealistically high, particularly in thick-walled shells or materials with considerable hardening (Hutchinson & Budiansky, 1976).

The documented superiority of J2DT in estimating the bifurcation point (Tuğcu, 1991; Blachut et al., 1996; Wang, et al., 2001) can be explained by the material stiffness moduli that J2DT employs, which are less stiff compared to the J2FT. This more compliant material behavior can be attributed to the development of corners in the yield surface of real materials when abrupt changes in stress direction occur, which was investigated in the 60s (Hecker,1972) and was observed experimentally more recently (Kuroda & Tvergaard, 1999; Kuwabara et al., 2000)

Budiansky (1959) argued for the applicability of J2DT for a range of problems with load paths which do not involve unloading, as the J2DT does not have such a condition. However, in the post-buckling of compressed shells, parts of the shell may unload. A hybrid approach has been suggested to overcome this issue, using the J2FT for tracing the primary equilibrium path of the structures, and the J2DT material moduli for estimating bifurcation. This method has been suggested in early works (Bushnell, 1974; Gellin, 1979), and used successfully in problems of structural instability of tubes under compressive loads (Ju & Kyriakides, 1991, 1992; Bardi et al., 2006; Corona et al., 2006; Peek & Hilberink, 2013). Still, it requires the use of two distinct constitutive laws for the same material within the analysis, while it may not allow for tracing consistently the post-buckling behavior, as the approach does not allow instantaneous jump to the non-trivial branch.

More advanced constitutive models have been proposed by (Christoffersen & Hutchinson, 1979; Gotoh, 1985; Goya & Ito, 1991) incorporating a yield surface with a vertex; a detailed overview is given in Schurig (2006). In particular, the J_2 corner theory, developed by Christoffersen & Hutchinson (1979), employs the rate form of the J2DT for a range of strain rate directions, elastic unloading within a conical yield surface, and partial loading in between, and has been successfully employed in problems of shear band formation (Christoffersen & Hutchinson, 1979; Needleman & Tvergaard, 1984), as well as in structural instability problems (Tvergaard, 1983a, 1983b; Giezen, 1988; Tvergaard & Needleman, 2000). However, the calibration and implementation of such models in an implicit finite element environment may become quite cumbersome, making their use unattractive for structural computations.

To circumvent the complexity of corner models, flow rules were suggested which mimic the increased plastic flow caused by yield surface corners, while maintaining the smooth shape of Von Mises yield surfaces. Hughes & Shakib (1986) developed an associative flow rule with increased plastic flow, with

a hardening modulus dependent on the direction of the strain increment. Yet, it demands significant hardening and no application in structural stability problems has been identified by the authors. Simo (1987) presented a non-associative flow rule which mimics the effect of a yield surface corner, applicable independently of the level of hardening. However, the corresponding instantaneous and linearized stiffness moduli were not presented, nor the model implementation for nonlinear hardening materials. This model was used by Rønning et al. (2010) for modeling the buckling of cruciform columns, and it was the basis for the non-associative models by (Kuroda & Tvergaard, 2001; Yoshida, 2017).

To inherit the effectiveness of J2DT in buckling predictions, some models were developed that employ its rate form, along with a smooth Von Mises yield surface. However, in this approach accounting for elastic unloading, creates a discontinuity in the production of plastic flow in directions tangent to the yield surface. To eliminate this discrepancy, Peek (2000) relaxed the demand for elastic unloading, allowing for some plastic deformation to take place for stress paths directed within the yield surface. In a different approach, Pappa & Karamanos (2016) maintained elastic unloading but modified the J2DT flow for a range of straining directions close to the yield-surface tangent so that plastic production is smoothly zeroed for tangent directions, but the ensuing strain-direction dependency was not fully incorporated in the formulation. These models were used to investigate the buckling response of metal tubes under compression.

The complexities and shortcomings of the above approaches motivate the development of the present model. It is a simple and effective constitutive model, which allows for (a) tracing the equilibrium path and (b) estimating accurately the structural instability of thick-walled shells loaded into the inelastic range.

A non-associative model (J2NA) is developed adopting a smooth yield surface, due to its robustness, combined with a two-branch flow rule. The first branch, activated for moderate deviations from proportional loading, employs the rate form of the J2DT, to inherit its effectiveness in structural instability predictions. The second branch, activated for larger deviations from proportional loading, is used for strain increment directions approaching the yield-surface-tangent. It is an extension of the approach by Simo (1987), mimicking the effect of a yield surface corner of semi-angle denoted as θ_{cr}, and it is adopted for its effectiveness and natural geometric interpretation. Fully elastic unloading is accounted for in strain-increment directions tangent and inward to the yield surface.

The capabilities of the constitutive model are demonstrated in the problem of instability of thick-walled metal tubes under axial compression. A material subroutine (UMAT) is developed and has been employed in ABAQUS/Standard to simulate the structural response and instability of thick-walled metal tubes under axial compression. Bifurcation estimates are compared with predictions from different constitutive models and with experimental results reported by Bardi & Kyriakides (2006). The model's behavior is shown to vary between the one predicted by the J2FT and the one associated with the J2DT, based on the model's material parameter (θ_{cr}). The effect of the model's features and of initial geometric imperfections on the simulated post-buckling behavior of thick-walled tubes is demonstrated.

2 Model formulation

A framework is presented for developing non-associative metal plasticity models, employing a smooth Von Mises yield surface. Modifying the rate form of the J2DT and introducing a non-associative hardening function $\bar{h}$ dependent on the loading history and the direction of the strain

rate, different amounts of allowable non-associative plastic straining can be implemented, resulting in stiffer or more compliant material behavior, without negating the requirement of elastic unloading.

For simulating the structural behavior and instability of thick-walled metal shells, a two branched definition is proposed for $\bar{h}$, so that the model can reliably trace the equilibrium path of compressed shells and consistently estimate bifurcation. The rate form of the J2DT is employed for small deviations from proportional loading, to capitalize on the good bifurcation predictions of this model, which are in agreement with available experimental data. In addition, a branch following the approach by (Simo, 1987) is used to moderate the non-associative straining for more pronounced deviations from proportional loading, due to its simplicity and its geometric interpretation that mimics the development of a yield surface vertex.

Preliminary calculations indicated that the direct use of either the J2DT or Simo's model individually may not result in both: (a) estimating instability and (b) tracing post-buckling behavior of thick-walled cylinders. By combining both models, as presented in the following, their desirable attributes are transferred into the present model.

2.1 A framework for non-associative plasticity models with a Von Mises yield surface

In the framework of incremental small-strain metal plasticity, the rate of stress $\dot{\boldsymbol{\sigma}}$ is related to the elastic strain rate $\dot{\boldsymbol{\varepsilon}}^e$ as follows:

$$\dot{\boldsymbol{\sigma}} = \mathbf{D}\dot{\boldsymbol{\varepsilon}}^e = \mathbf{D}(\dot{\boldsymbol{\varepsilon}} - \dot{\boldsymbol{\varepsilon}}^p) = \mathbf{D}\dot{\boldsymbol{\varepsilon}} - \mathbf{D}\dot{\boldsymbol{\varepsilon}}^p \tag{1}$$

where $\mathbf{D}$ is the fourth-order elastic stiffness tensor, $\dot{\boldsymbol{\varepsilon}}$ is the rate of total strain, $\dot{\boldsymbol{\varepsilon}}^e$ is the rate of elastic strain and $\dot{\boldsymbol{\varepsilon}}^p$ is the (deviatoric) plastic strain rate. The elastic rigidity $\mathbf{D}$ can be expressed as:

$$\mathbf{D} = 2G\,\mathbf{I}^{dev} + 3K\,\mathbf{I}^{vol} \tag{2}$$

where G is the shear modulus and K is the bulk modulus. $\mathbf{I}^{dev}$, $\mathbf{I}^{vol}$ are the deviatoric and volumetric fourth-order unit tensors, whose Cartesian components are:

$$I_{ijkl}^{dev} = \frac{1}{2}\left(\delta_{ik}\delta_{jl} + \delta_{il}\delta_{jk}\right) - \frac{1}{3}\delta_{ij}\delta_{kl} \tag{3}$$

$$I_{ijkl}^{vol} = \frac{1}{3}\delta_{ij}\delta_{kl} \tag{4}$$

The rate of plastic strain $\dot{\mathbf{e}}^p$ of the J2DT, as reported by Chakrabarty (2006) is:

$$\dot{\mathbf{e}}^p = \frac{3}{2}\left(\frac{\dot{\varepsilon}_q}{q} - \frac{\varepsilon_q \dot{q}}{q^2}\right)\mathbf{s} + \frac{3}{2}\frac{\varepsilon_q}{q}\dot{\mathbf{s}} \tag{5}$$

where $\mathbf{s} = \mathbf{I}^{dev}\boldsymbol{\sigma}$ is the deviatoric part of the stress tensor, ε_q is the (accumulated) equivalent plastic strain, $q = \sqrt{3/2}\,\|\mathbf{s}\|$ is the equivalent Von Mises stress, with $\|\mathbf{s}\| = \sqrt{\mathbf{s}\cdot\mathbf{s}}$ being the norm of $\mathbf{s}$, and their rates, indicated by a superimposed dot: $\dot{\mathbf{s}}$, $\dot{\varepsilon}_q$ and $\dot{q}$. By further enforcing consistency with a Von Mises yield surface in (5), which implies ($\dot{\varepsilon}_q = \dot{q}/H$), the flow rule of the J2DT as presented by (Goya & Ito, 1991; Pappa & Karamanos, 2016) can be obtained.

Considering these definitions, one may readily show that $\dot{q} = \sqrt{3/2}\,\mathbf{s}\cdot\dot{\mathbf{s}}/\|\mathbf{s}\|$, and $\dot{\mathbf{s}} = 2G(\dot{\mathbf{e}} - \dot{\mathbf{e}}^p)$ with $\dot{\mathbf{e}} = \mathbf{I}^{dev}\dot{\boldsymbol{\varepsilon}}$. Inserting those in (5) and rearranging, the plastic strain rate adopted in the present formulation is obtained:

$$\dot{\mathbf{e}}^p = \sqrt{3/2}\,\dot{\varepsilon}_q\mathbf{n} + \frac{[\mathbf{I}^{dev} - \mathbf{n}\otimes\mathbf{n}]\dot{\mathbf{e}}}{1 + \bar{h}/3G} \tag{6}$$

where $\mathbf{n} = \mathbf{s}/\|\mathbf{s}\|$ is the unit tensor in the direction of $\mathbf{s}$**.** The plastic strain rate comprises two components: one in the direction of the tensor $\mathbf{n}$ and one in the direction $[\mathbf{I}^{dev} - \mathbf{n}\otimes\mathbf{n}]\dot{\mathbf{e}}$, which is perpendicular to $\mathbf{n}$, in the direction defined by the strain rate. The function $\bar{h}$ is a non-associative-hardening parameter, whose definition is discussed in subsection 2.2, that moderates the amount of plastic straining perpendicular to $\mathbf{n}$. In (6), the rate of equivalent plastic strain is defined as $\dot{\varepsilon}_q =$

$\sqrt{2/3}\,\mathbf{n}\cdot\dot{\mathbf{e}}^p$, a definition also adopted by Simo (1987), which for proportional loading is equivalent to its counterpart in J2FT ($\dot{\varepsilon}_q = \sqrt{2/3}\sqrt{\dot{\mathbf{e}}^p\cdot\dot{\mathbf{e}}^p}$). The flow rule (6) can be rewritten in the following, more convenient, geometric form, which is used more extensively in the numerical integration of the model, described in section 3:

$$\dot{\mathbf{e}}^p = \sqrt{3/2}\,\dot{\varepsilon}_q\,\mathbf{n} + \frac{\|\dot{\mathbf{e}}\|\sin\theta}{1+\bar{h}/3G}\mathbf{m} \tag{7}$$

In (7), θ is the angle defined by the strain rate $\dot{\mathbf{e}}$ and the tensor $\mathbf{n}$, shown in Figure 1, analytically expressed as:

$$\cos\theta = \frac{\mathbf{n}\cdot\dot{\mathbf{e}}}{\|\dot{\mathbf{e}}\|} \tag{8}$$

and $\mathbf{m}$ is the unit deviatoric tensor perpendicular to $\mathbf{n}$, in the direction of the strain rate

$$\mathbf{m} = \frac{(\mathbf{I}^{dev}-\mathbf{n}\otimes\mathbf{n})\dot{\mathbf{e}}}{\|(\mathbf{I}^{dev}-\mathbf{n}\otimes\mathbf{n})\dot{\mathbf{e}}\|} = \frac{(\mathbf{I}^{dev}-\mathbf{n}\otimes\mathbf{n})\dot{\mathbf{e}}}{\|\dot{\mathbf{e}}\|\sin\theta} \tag{9}$$

Yielding is defined with respect to a Von Mises yield function with nonlinear isotropic hardening:

$$F(\boldsymbol{\sigma},\varepsilon_q) = \frac{\sqrt{2/3}}{2G}\left[q-k(\varepsilon_q)\right] = \frac{\|\mathbf{s}\|}{2G} - \frac{\sqrt{2/3}\,k(\varepsilon_q)}{2G} \quad = 0 \tag{10}$$

where $k(\varepsilon_q)$ is the material yield stress in uniaxial tension, that defines the size of the yield surface as a function of the (accumulated) equivalent plastic strain ε_q. The above expression for the Von Mises yield criterion is chosen because it scales down the yield surface to the deviatoric strain space, so that all the strain components, the shape of the yield surface and their relative size and geometry can be presented in the same graph (e.g. Figures 1, 7, 8). Hence, tensors $\mathbf{n}$, $\mathbf{m}$ are the unit tensors normal and tangent to the Von Mises yield surface respectively, and eq. (7) demonstrates the non-associative nature of the present model, with the increased plastic flow moderated by $\bar{h}$.

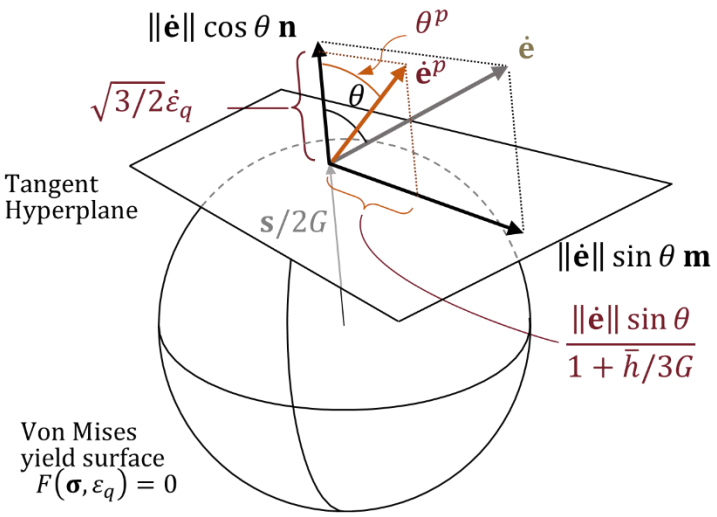

Figure 1 Schematic representation of key tensors in the deviatoric hyperplane and angles $\boldsymbol{\theta}$, $\boldsymbol{\theta^p}$.

Enforcing consistency $(\dot{F} = 0)$, and using (1) and (7), the equivalent plastic strain rate is expressed similarly to the J2FT :

$$\dot{\varepsilon}_q = \sqrt{2/3}\frac{1}{1+H/3G}(\mathbf{n}\cdot\dot{\mathbf{e}}) \tag{11}$$

where $H = dk/d\varepsilon_q$ is the material isotropic hardening modulus. Using equations (1), (7) and (11), the instantaneous rigidity tensor for this model is readily calculated as

$$\mathbf{D}_{ep} = 3K\,\mathbf{I}^{vol} + \frac{2G}{1+3G/\bar{h}}\,\mathbf{I}^{dev} - \left(\frac{2G}{1+H/3G} - \frac{2G}{1+\bar{h}/3G}\right)(\mathbf{n}\otimes\mathbf{n}) \tag{12}$$

2.2 Definition of the function $\bar{h}$

The choice of $\bar{h}$ is of key importance in this model, leading to stiffer or more compliant material behavior. Table 2 shows that the appropriate selection of $\bar{h}$, allows the model to mimic different material models available in the literature.

To incorporate elastic unloading together with the selected flow rule, continuity of the production of plastic strain must be assured (Figure 2), as noted by Peek (2000) and Pappa & Karamanos (2016). This implies that no plastic strain should be produced for strain rates directed tangent to the yield surface ($\theta \to \pi/2$), which creates demand (13) for the function $\bar{h}$:

$$\lim_{\theta\to(\pi/2)^-} \|\dot{\mathbf{e}}^p\|/\|\dot{\mathbf{e}}\| = 0 \;\Rightarrow \lim_{\theta\to(\pi/2)^-} \bar{h} \to +\infty \tag{13}$$

Therefore, $\bar{h}$ must depend on the direction of the strain rate (θ), which implies that the rigidity tensor (12) at a material point is not fully defined by its loading history, but the strain rate direction must also be known. This is a manifestation of the nonlinear dependence of the stress rate on the strain rate, characteristic in pseudo-corner models.

Table 1 Summary of the elastoplastic constitutive model

(1) Linear isotropic stress/strain relations

$$\mathbf{s} = 2G[\mathbf{e} - \mathbf{e}^p]$$
$$tr\ \boldsymbol{\sigma} = 3K\ tr\ \boldsymbol{\varepsilon}$$

(2) Yield condition

$$F(\boldsymbol{\sigma}, \varepsilon_q) = \frac{1}{2G}\left[\|\mathbf{s}\| - \sqrt{2/3}\, k(\varepsilon_q)\right]$$
$$\dot{\varepsilon}_q = \sqrt{2/3}\, \mathbf{n} \cdot \dot{\mathbf{e}}^p$$
$$\mathbf{n} = \mathbf{s}/\|\mathbf{s}\|$$

(3) Flow rule

$$\dot{\mathbf{e}}^p = \sqrt{3/2}\, \dot{\varepsilon}_q\, \mathbf{n} + \frac{\|\dot{\mathbf{e}}\| \sin\theta}{1 + \bar{h}/3G}\, \mathbf{m}$$
$$\mathbf{m} = \frac{(\mathbf{I}^{dev} - \mathbf{n} \otimes \mathbf{n})\dot{\mathbf{e}}}{\|(\mathbf{I}^{dev} - \mathbf{n} \otimes \mathbf{n})\dot{\mathbf{e}}\|}$$
$$\cos\theta = \mathbf{n} \cdot \dot{\mathbf{e}}/\|\dot{\mathbf{e}}\|$$
$$\cos\theta^p = \mathbf{n} \cdot \dot{\mathbf{e}}^p/\|\dot{\mathbf{e}}^p\|$$
$$h = k(\varepsilon_q)/\varepsilon_q$$

1st branch: $\bar{h} = h \quad \& \quad \theta^p(\bar{h}) \le \theta_{cr}$

2nd branch: $\theta^p = \theta_{cr} \to \bar{h}(\theta_{cr}) > h$

(4) Kuhn-Tucker loading/unloading conditions

$$\dot{\varepsilon}_q \ge 0, \qquad F(\boldsymbol{\sigma}, \varepsilon_q) \le 0, \qquad \dot{\varepsilon}_q F(\boldsymbol{\sigma}, \varepsilon_q) = 0$$

(5) Plastic consistency in loading ($\dot{\varepsilon}_q > 0$)

$$\dot{\varepsilon}_q = \sqrt{2/3}\, \frac{1}{1 + H/3G}\, (\mathbf{n} \cdot \dot{\mathbf{e}})$$

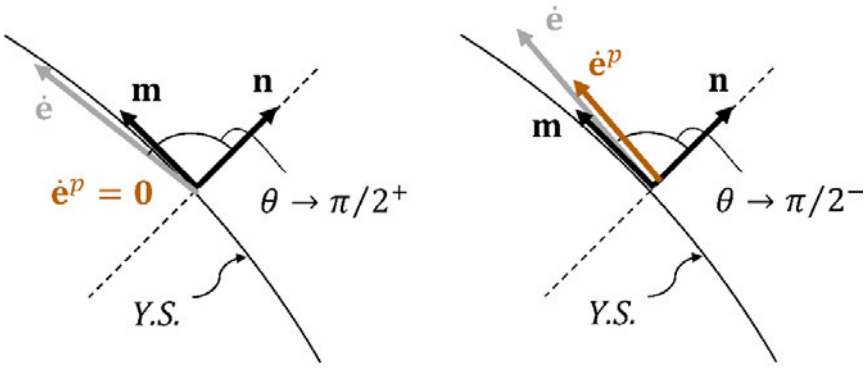

Figure 2 Discontinuity of plastic production for straining directions tangent to the yield surface

The present model (J2NA) adopts a two-branch definition for the non-associate hardening parameter $\bar{h}$. For small deviations from proportional loading, $\bar{h} = h = k(\varepsilon_q)/\varepsilon_q$, and the model's flow rule coincides with the J2DT, aspiring to inherit its superiority in estimating bifurcation. A second branch is necessary to comply with the limitations imposed by elastic unloading, so for larger deviations from proportional loading, up to loading tangent to the yield surface, the model is chosen to follow the flow proposed by Simo (1987). This branch mimics the effect of a conical yield surface vertex of semi-angle θ_{cr} in the direction of the stress deviator: it constrains the plastic strain rate to lie within the forward cone of normals of the vertex, as shown in Figure 3. This is interpreted as $(\theta^p \leq \theta_{cr})$, where θ^p is the angle formed by the yield surface normal and the plastic strain rate (Figure 1), analytically expressed as:

$$\cos\theta^p = \frac{\mathbf{n} \cdot \dot{\mathbf{e}}^p}{\|\dot{\mathbf{e}}^p\|} \tag{14}$$

From (7) and (14), it is deduced that θ^p is a decreasing function of $\bar{h}$, which allows for the two branches of the model to be reduced to the following definition.

$$\{\bar{h} \geq h = k(\varepsilon_q)/\varepsilon_q \quad \text{so that} \quad \theta^p \leq \theta_{cr}\} \tag{15}$$

A summary of the model is given in Table 1. In the rate form, the present definition of $\bar{h}$ (eq. 15), can be expressed in the form presented in Table 2, which demonstrates the compliance with requirement for continuity of plastic production (eq.13).

The value of parameter θ_{cr} can be determined from experiments involving non-proportional loading, like the ones described by (Rønning et al., 2010; Yoshida & Tsuchimoto, 2018). In those experiments, tension is applied first to a tubular specimen beyond the yield point, followed by combined tension and torque load increments, producing a non-proportional stress path. The value of θ_{cr} can then be obtained from the direction of the corresponding plastic strain increments, calculated using equations (14), (15). In an analogous manner, the parameter θ_{cr} can also be calculated from biaxial experiments on cruciform specimens (Kuroda & Tvergaard, 1999; Kuwabara, et al., 2000), in which non-proportionality is induced in the second loading stage by applying load increments in different directions.

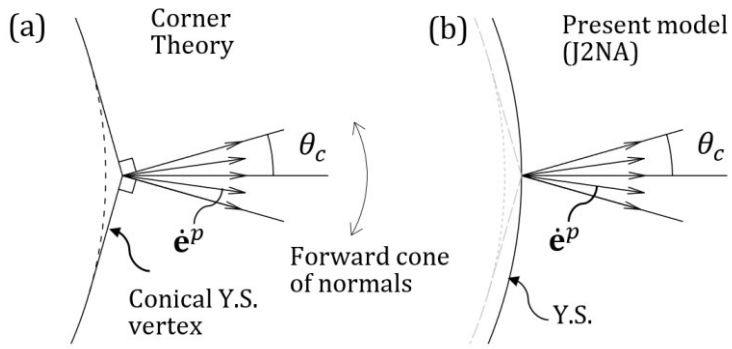

Figure 3 Yield surface and directions of plastic strain rate in a) corner models and (b) non-associative model

Table 2 Expressing different models (in their rate form) by different definitions of $\bar{h}$

J_2 Flow – Associative model	$\bar{h} \to +\infty$
J_2 Deformation Theory Rate Form	$\bar{h} = h = k(\varepsilon_q)/\varepsilon_q$
Pappa & Karamanos (2016)	$\bar{h} = [E \sin^n \theta + h]/[1 - \sin^n \theta]$
Simo (1987)	$\bar{h} = Hc + 3G(c-1), \quad c = \tan\theta/\hat{\delta}(\theta),$ $\hat{\delta}(\theta) = \tan(\max(\theta, \theta_{cr}))$
Present model	$\bar{h} = \max\begin{Bmatrix} k(\varepsilon_q)/\varepsilon_q \\ Hc + 3G(c-1) \end{Bmatrix}, c = \tan\theta \,/\, \tan\theta_{cr}$

2.3 Plastic production ratio and comparison with other models

A qualitative comparison between different corner and pseudo-corner models can be made using the plastic production $w^*(\theta, \varepsilon_q)$ and the plastic angle $\theta^p(\theta, \varepsilon_q)$ associated with each model. The former, introduced by Hughes & Shakib (1986), expresses the amount of plastic strain caused by a strain rate $\dot{\mathbf{e}}$, depending on its direction (angle θ), and is defined as:

$$w^*(\theta, \varepsilon_q) = \frac{\|\dot{\mathbf{e}}^p\|}{\dfrac{\|\dot{\mathbf{e}}\|}{1 + H/3G}} \tag{16}$$

The plastic angle θ^p is an additional measure for describing the behavior of a model, stemming from the non-associative nature of the majority of the models and it expresses the angle the plastic strain rate forms with the yield surface normal, defined in (14) depending on the direction of the (total) strain rate. Analytical expressions for these measures, for several flow rules, can be found in Table 4.

The behavior of the models depends on the loading history of the material; therefore, we consider here a specific material point, loaded proportionally to its current stress state, well into the inelastic range. The material properties and state variables of the material point under consideration are given in Table 3.

Table 3 Material properties and state variables at current loading state

Young's Modulus	$E = 194\ GPa$
Poisson's Ratio	$\nu = 0.3$
Equivalent plastic strain	$\varepsilon_q = 1.6\%$
Von Mises Stress	$k = 710\ MPa$
Hardening modulus	$H/E = 2\%$
Angle parameter [2]	$\theta_{cr} = \pi/4$

In Figures 4 and 5 the plastic production and plastic angles are plotted with respect to the angle θ for the proposed model and several other models available in the literature. For the J_2 corner theory two curves are plotted, each one representing a family of flow rules proposed by Christoffersen & Hutchinson (1979). For proportional loading ($\theta = 0$), all models predict the same plastic production as the J2FT, since all models must be able to replicate identically a proportional loading experiment, i.e., a uniaxial test. As non-proportionality increases, plastic production in all models is higher than the one predicted by the J2FT, corresponding to more compliant responses. All models that account for fully elastic unloading produce zero plastic strain for strain rates directed tangent to their respective yield surfaces. Those directions correspond to $\theta = \pi/2$ for the models employing a Von Mises yield surface, and to $\theta = \pi - \theta_c$ for the models which employ a yield surface vertex, such as the J_2 corner theory. The value of θ_c is given in Table 4.

The J_2 corner theory, the models by Peek (2000) and Pappa & Karamanos (2016) and the present model, all exhibit a response similar with the J2DT for a certain range of straining directions (θ). Each of them uses a second branch with the purpose of gradually suppressing plastic production for strain rate directions that approach the tangent to the yield surface. This is a major feature that differentiates each model with respect to the others. All models incorporate a maximum allowable

[2] Applicable for the models by Simo (1987), Hughes & Shakib (1986) and the present model

angle θ^p which the plastic strain rate may not exceed, but its value and the range of straining directions θ for which this angle is activated is different for each model.

Additionally, at first yield the J2DT has an essentially associative behavior, allowing for plastic straining only in the direction of the deviatoric stress. Progressively, as plastic strain accumulates, increasing amounts of non-associative plastic straining are produced for a given angle θ, meaning that both plastic production and plastic angle increase (Figure 6). For large values of accumulated plastic strain ε_q this behavior becomes similar to the first branch of the model proposed by Simo (1987). This gradually more compliant behavior of the rate form of the J2DT leads to lower bifurcation estimates for thick-walled shells and justifies its use in several constitutive models which inherit its capability for providing reliable buckling predictions.

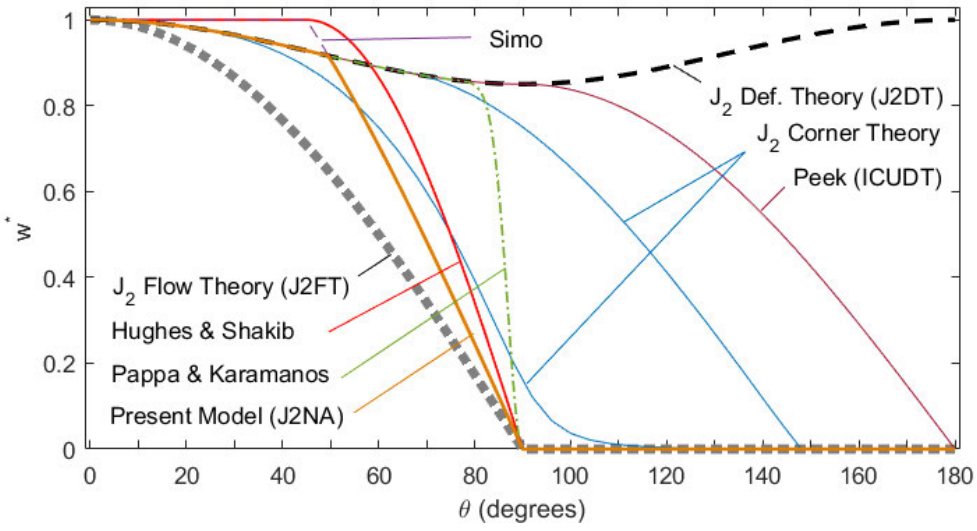

Figure 4 Normalized plastic production ration with respect to the direction of the strain rate (angle $\boldsymbol{\theta}$)

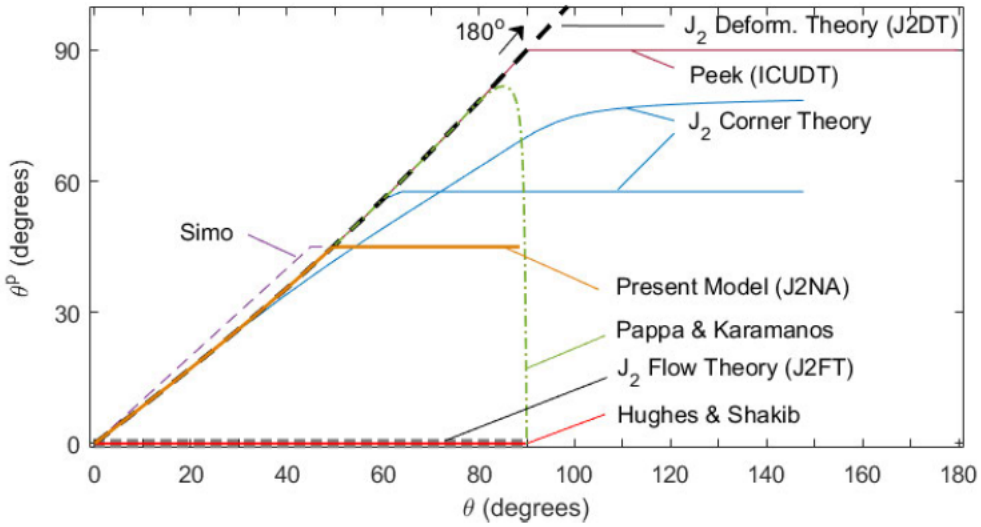

Figure 5 Direction of plastic strain rate angle $\boldsymbol{\theta^p}$ with respect to the direction of the total strain rate (angle $\boldsymbol{\theta}$)

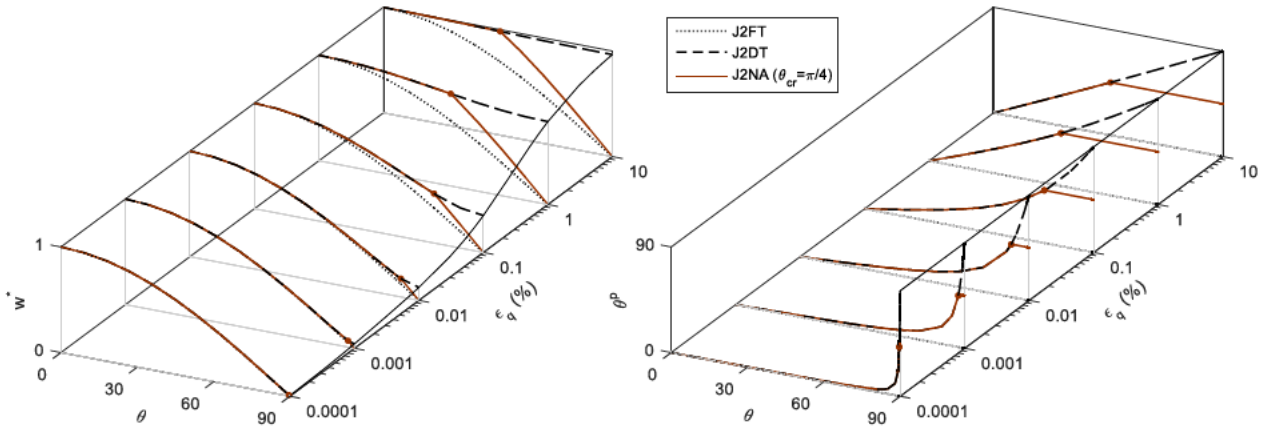

Figure 6 Evolution of plastic production $\boldsymbol{w^*}$ with increasing plastic deformation; evolution of plastic strain rate angle $\boldsymbol{\theta^p}$, with increasing plastic deformation.

Table 4 Plastic production and plastic angle for different models

	Plastic Production $w^*(\theta, \varepsilon_q)$	**Plastic Angle** $\tan\theta^p(\theta, \varepsilon_q)$	**Details**
J_2 Flow theory (associative)	$\cos\theta$	0	
Hughes and Shakib (1987)	$\cos\psi$	0	$\psi = \max\left\{0, \quad \frac{\pi}{2}\frac{(\theta-\theta_{cr})}{(\pi/2-\theta_{cr})}\right\}$
Simo (1987)	$\cos\theta\sqrt{1+\hat{\delta}^2}$	$\hat{\delta}(\theta)$	$\hat{\delta}(\theta) = \tan(\min\{\theta, \theta_{cr}\})$
J_2 Deform. Theory (Total Strain Theory)	$\sqrt{\cos^2\theta + c^2\sin^2\theta}$	$c\tan\theta$	$c = [1+H/3G] \,/\, [1+h/3G]$
Pappa & Karamanos (2016)	$\sqrt{\cos^2\theta + c^2\sin^2\theta}$	$c\tan\theta$	$c = [1+H/3G] \,/\, [1+h_{PnK}/3G]$ $h_{PnK} = [E\sin^n\theta + h]/[1-\sin^n\theta]$
Peek (2000)	$\sqrt{\cos^2(\theta^{ICU}) + c^2\sin^2\theta}$	$c\tan\theta^{ICU}$	$c = [1+H/3G] \,/\, [1+h/3G]$ $\theta^{ICU} = min(\theta, \pi/2)$
J_2 Corner Theory	$\frac{\sqrt{x^2+(yz)^2}}{\sqrt{(1+x)^2+[(1+y)z]^2}}$	$\sqrt{H/h}\tan\phi^{CH}$	$x = \frac{3G}{H}f(\theta^{CH})[1+k(\theta^{CH})\tan\theta^{CH}]$ $y = \frac{3G}{h}f(\theta^{CH})[1-k(\theta^{CH})\cot\theta^{CH}]$ $z = \sqrt{h/H}\tan\theta^{CH}$
Family 1.	$f = f(\theta^{CH})$ $= \begin{cases} \cos^2\left[\frac{\pi}{2}\frac{(\theta^{CH}-\theta_0)}{(\theta_c-\theta_0)}\right], & 0 \le \theta^{CH} \le \theta_0 \\ & \theta_0 \le \theta^{CH} \le \theta_c \\ 0, & \theta_c \le \theta^{CH} \le \pi \end{cases}$ $k(\theta^{CH}) = -f'/(2f)$		with $\tan\theta = \frac{1+y}{1+x}\sqrt{h/H}\tan\theta^{CH}$ $\phi^{CH} = \theta^{CH} - \tan^{-1}[k(\theta^{CH})]$
Family 2.	$f(\theta^{CH}) = \left[g(\phi^{CH})[1+l(\phi^{CH})]\right]^{-1}$ $k(\theta^{CH}) = l(\phi^{CH})$ with $g(\phi^{CH}) = \begin{cases} 1, & 0 \le \phi^{CH} \le \theta_0 \\ (1-\bar{\phi}^m)^{-2}, & \theta_0 \le \phi^{CH} \le \theta_\pi \end{cases}$ $l(\phi^{CH}) = g'/(2g)$ And $\bar{\phi} = (\phi-\theta_0)/(\theta_\pi-\theta_0), m \ge 2$		$\tan\theta_c = -\sqrt{H/h}\frac{\sigma_0}{\sqrt{\sigma_e^2-\sigma_0^2}}$ where σ_0 is the yield stress of the material and σ_e is the current mises stress of the material and $\theta_0 \le \theta_c - \pi/2$ is the angle θ^{CH} cutoff, following which the models cease to follow the deformation theory flow rule
Present model	$\sqrt{\cos^2\theta + c^2\sin^2\theta}$	$\min\{c\tan\theta, \tan\theta_{cr}\}$	$c = [1+H/3G] \,/\, [1+h/3G]$

3 Numerical implementation

A stress update algorithm (or integration scheme) is developed accounting for the particular features of the present model. A geometric approach, similar to the one developed by Simo (1987), is adopted for the integration of the governing equations, while modifications are introduced intended to account for nonlinear material hardening, and for the dependence the model exhibits on the direction of the strain increment. Appropriate mathematical manipulations reduce the integration of the model to the solution of a single equation of a scalar unknown, irrespective of the material hardening rule, just as in the case of J2FT. This is in contrast to previous formulations which lead to more complicated iterative solutions (Rønning et al., 2010), some are confined to linear hardening (Hughes & Shakib, 1986; Simo, 1987) or do not fully account for the angle dependence (Pappa & Karamanos, 2016). Both the integration and linearization schemes fully account for the dependence on the strain direction angle θ.

3.1 Backward-Euler stress update algorithm

For any material point at pseudo-time t_n the stress $\boldsymbol{\sigma}_n$ and strain $\boldsymbol{\varepsilon}_n$ are known, as well as the equivalent plastic strain $\varepsilon_{q|n}$ (internal variable). At pseudo-time $t_{n+1} = t_n + \Delta t$, a strain increment $\Delta\boldsymbol{\varepsilon} = \boldsymbol{\varepsilon}_{n+1} - \boldsymbol{\varepsilon}_n$ leads to changes in the material stress state $\boldsymbol{\sigma}_{n+1}$ and internal variable $\varepsilon_{q|n+1}$, which are calculated by integrating the plasticity constitutive model in the pseudo-time increment Δt.

An elastic predictor–plastic corrector scheme is adopted: an elastic-predictor step, leading to a stress state outside the yield surface, is followed by a plastic-corrector step, which enforces consistency and returns the stress to the updated yield surface. The elastic predictor $\boldsymbol{\sigma}^e$ assumes a purely elastic trial stress and is decomposed as follows:

$$\boldsymbol{\sigma}^e = \boldsymbol{\sigma}_n + \mathbf{D}\Delta\boldsymbol{\varepsilon} = \mathbf{s}^e - p^e\mathbf{I} \tag{17}$$

where

$$\mathbf{s}^e = \mathbf{I}^{dev}\boldsymbol{\sigma}^e = \mathbf{s}_n + 2G\Delta\mathbf{e} \tag{18}$$

$$p^e = -1/3\,(\mathbf{I}\cdot\boldsymbol{\sigma}^e) = p_n - K(\mathbf{I}\cdot\Delta\boldsymbol{\varepsilon}) \tag{19}$$

Furthermore, $\Delta\mathbf{e} = \mathbf{I}^{dev}\Delta\boldsymbol{\varepsilon}$ is the deviatoric part of the strain increment**,** p_n and $\mathbf{s}_n$ are respectively the hydrostatic pressure and the stress deviator at the beginning of the increment ($\boldsymbol{\sigma}_n = \mathbf{s}_n - p_n\mathbf{I}$). The Von Mises stress at the beginning of the strain increment (q_n) and at the elastic predictor state (q^e) are respectively defined as:

$$q_n = \sqrt{3/2}\,\sqrt{\mathbf{s}_n\cdot\mathbf{s}_n} = \sqrt{3/2}\,\|\mathbf{s}_n\| \tag{20}$$

$$q^e = \sqrt{3/2}\,\sqrt{\mathbf{s}^e\cdot\mathbf{s}^e} = \sqrt{3/2}\,\|\mathbf{s}^e\| \tag{21}$$

If the trial stress violates the yield condition, elastic-plastic straining is accounted for, and the new stress state is calculated by including the plastic correction phase

$$\boldsymbol{\sigma}_{n+1} = \boldsymbol{\sigma}_n + \mathbf{D}\,(\Delta\boldsymbol{\varepsilon} - \Delta\mathbf{e}^p) = \boldsymbol{\sigma}^e - 2G\Delta\mathbf{e}^p \tag{22}$$

The stress at pseudo-time t_{n+1} is decomposed into

$$\boldsymbol{\sigma}_{n+1} = -p_{n+1}\mathbf{I} + \mathbf{s}_{n+1} \tag{23}$$

where $-p_{n+1}\mathbf{I}$ and $\mathbf{s}_{n+1}$ are the hydrostatic and deviatoric parts of the final stress $\boldsymbol{\sigma}_{n+1}$**,** with

$$p_{n+1} = -\frac{1}{3}(\mathbf{I}\cdot\boldsymbol{\sigma}_{n+1}) = p^e \tag{24}$$

$$\mathbf{s}_{n+1} = \mathbf{I}^{dev}\boldsymbol{\sigma}_{n+1} = \mathbf{s}^e - 2\mathrm{G}\Delta\mathbf{e}^p \tag{25}$$

Enforcing the consistency condition (10) at the end of the increment (t_{n+1}):

$$F\big(\boldsymbol{\sigma}_{n+1}, \Delta\varepsilon_q\big) = \frac{\sqrt{\mathbf{s}_{n+1}\cdot\mathbf{s}_{n+1}}}{2G} - \frac{\sqrt{2/3}\,k\big(\varepsilon_{q|n} + \Delta\varepsilon_q\big)}{2G} = \sqrt{2/3}\,\frac{q_{n+1} - k_{n+1}}{2G} = 0 \tag{26}$$

where $\Delta\varepsilon_q$ is the equivalent plastic strain increment. The corresponding plastic strain increment $\Delta\mathbf{e}^p$ is calculated using a backward-Euler integration of equation (7):

$$\Delta\mathbf{e}^p = \sqrt{3/2}\,\Delta\varepsilon_q\,\mathbf{n}_{n+1} + \frac{\|\Delta\mathbf{e}\|\sin\theta}{1+\bar{h}_{n+1}/3G}\,\mathbf{m}_{n+1} \tag{27}$$

where the direction angle $\theta = \theta_{n+1}$ for simplicity. The unit deviatoric tensor normal to the yield surface and the one tangential to it, in the direction of the strain increment, at the beginning and the end of the increment (Figure 7) are respectively defined as:

$$\mathbf{n}_n = \frac{\mathbf{s}_n}{\|\mathbf{s}_n\|}, \qquad \mathbf{m}_n = \frac{[\mathbf{I}^{dev} - \mathbf{n}_n \otimes \mathbf{n}_n]\,\Delta\mathbf{e}}{\|[\mathbf{I}^{dev} - \mathbf{n}_n \otimes \mathbf{n}_n]\,\Delta\mathbf{e}\,\|} \tag{28}$$

$$\mathbf{n}_{n+1} = \frac{\mathbf{s}_{n+1}}{\|\mathbf{s}_{n+1}\|}, \qquad \mathbf{m}_{n+1} = \frac{[\mathbf{I}^{dev} - \mathbf{n}_{n+1} \otimes \mathbf{n}_{n+1}]\,\Delta\mathbf{e}}{\|[\mathbf{I}^{dev} - \mathbf{n}_{n+1} \otimes \mathbf{n}_{n+1}]\,\Delta\mathbf{e}\,\|} \tag{29}$$

while the unknown tensors $\mathbf{n}_{n+1}$, $\mathbf{m}_{n+1}$ can be expressed in terms of $\mathbf{n}_n$, $\mathbf{m}_n$ using the following geometric relation identified by Simo (1987):

$$\mathbf{n}_{n+1} = \quad \cos\zeta\,\mathbf{n}_n + \sin\zeta\,\mathbf{m}_n \tag{30}$$

$$\mathbf{m}_{n+1} = -\sin\zeta\,\mathbf{n}_n + \cos\zeta\,\mathbf{m}_n \tag{31}$$

In the above expression, the angle ζ is represented geometrically in Figure 7, together with angles ζ^*, ζ^e, θ, θ_n, θ^e, θ^p, that are formed by the key tensors and are involved in subsequent operations. Furthermore, geometry dictates:

$$\zeta = \zeta^e - \zeta^* \tag{32}$$

$$\theta = \theta_{n+1} = \theta^e + \zeta^* = \theta_n - \zeta \tag{33}$$

where

$$\cos\zeta^e = \frac{\mathbf{s}_n \cdot \mathbf{s}^e}{\|\mathbf{s}_n\|\|\mathbf{s}^e\|}, \qquad \cos\theta^e = \frac{\Delta\mathbf{e} \cdot \mathbf{s}^e}{\|\Delta\mathbf{e}\|\|\mathbf{s}^e\|} \tag{34}$$

Multiplying (25) by $\mathbf{n}_{n+1}$ and $\mathbf{m}_{n+1}$, the following relations are obtained:

$$q^e\cos\zeta^* = q_{n+1} + 3G\Delta\varepsilon_q \tag{35}$$

$$q^e \sin\zeta^* = \sqrt{2/3}\frac{3G\|\Delta\mathbf{e}\|\sin\theta}{1+\bar{h}_{n+1}/3G} \tag{36}$$

Equations (26), (33), (35), (36) constitute a system of 4 equations with 5 unknowns: q_{n+1}, $\Delta\varepsilon_q$, ζ^*, θ, and $\bar{h}_{n+1}$. The extra equation necessary for the solution is the definition of $\bar{h}$, which is different in each branch of the present model. The solution procedure for the system is described in the next paragraphs for each branch. The implementation of the above formulation for an explicitly chosen function $\bar{h}(\varepsilon_q,\theta)$ which may be chosen to mimic the behavior of various models in the literature is further considered in Appendix I. An enhancement of this solution procedure for implementation in shell elements is included in Appendix II.

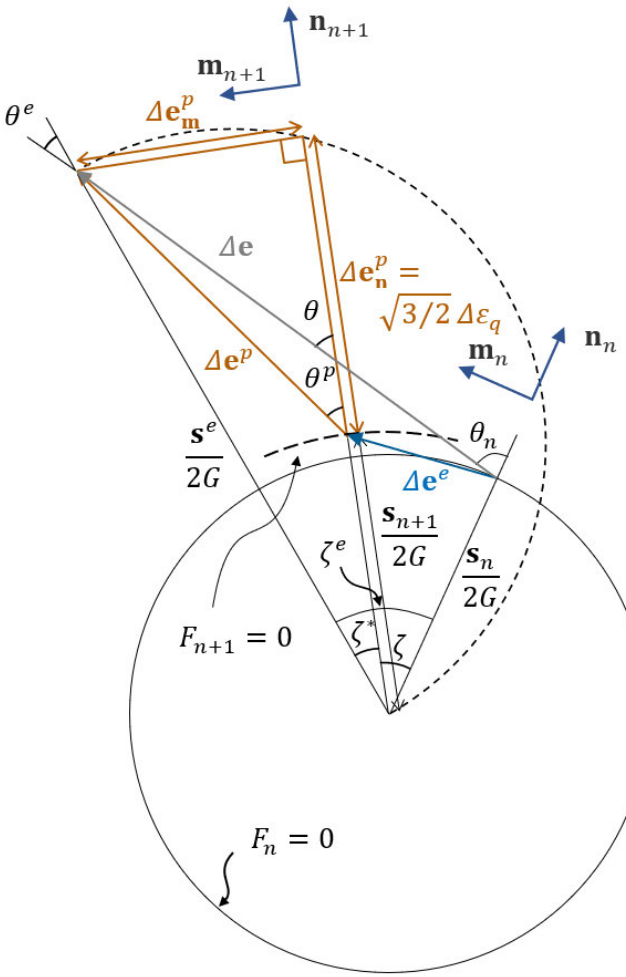

Figure 7 Geometric representation of the return mapping of a non-associative model

3.2 First branch of the model

In the first branch of the model, the parameter $\bar{h} = \bar{h}(\Delta\varepsilon_q)$ is defined as follows, independent of θ:

$$\bar{h}_{n+1} = k_{n+1}/\varepsilon_{q|n+1} \tag{37}$$

Thus, equation (36) together with (37) can be used to express $\zeta^*(\Delta\varepsilon_q)$ as a function of the equivalent plastic strain $\Delta\varepsilon_q$, as follows:

$$\tan\zeta^* - \frac{\sin\theta^e}{\frac{\|\mathbf{s}^e\|}{2G\|\Delta\mathbf{e}\|}\left[1+\frac{h_{n+1}}{3G}\right]-\cos\theta^e} = 0 \tag{38}$$

Treating only $\Delta\varepsilon_q$ as the primary unknown, equations (26) and (37) can be used to eliminate q_{n+1}, ζ^* from (36) resulting in a single scalar equation (39) of the equivalent plastic strain increment $F_{p1}(\Delta\varepsilon_q) = 0$, as in the case of J2FT.

$$F_{p1}(\Delta\varepsilon_q) = 1 + \left[\frac{\sin\theta^e}{\frac{\|\mathbf{s}^e\|}{2G\|\Delta\mathbf{e}\|}\left[1+\frac{h_{n+1}}{3G}\right]-\cos\theta^e}\right]^2 - \left[\frac{q^e}{k_{n+1}+3G\Delta\varepsilon_q}\right]^2 = 0 \tag{39}$$

The above equation (39) can be solved using a local Newton scheme and all necessary derivatives are provided in Appendix I. When $\Delta\varepsilon_q$ is found all remaining parameters are updated and the plastic corrector is computed from (27). At this stage, the plastic strain angle θ^p is compared to θ_{cr}: if $\theta^p \leq \theta_{cr}$ the integration procedure is complete, else, the solution is discarded, and the integration scheme of the second branch is used. A summary of this integration procedure is given in Table 5.

3.3 Second branch of the model

In cases where the first branch of the model leads to plastic strain increment angle θ^p_{br1} greater than the semi-angle θ_{cr} of the simulated vertex ($\theta^p_{br1} > \theta_{cr}$), the second branch is activated. In this case, the plastic strain increment is constrained to form an angle $\theta^p = \theta_{cr}$ with the deviatoric stress in the converged state, so that:

$$\tan\theta^p = \frac{\mathbf{m}_{n+1}\cdot \Delta\mathbf{e}^p}{\mathbf{n}_{n+1}\cdot \Delta\mathbf{e}^p} = \tan\theta_{cr} \tag{40}$$

Using (27), (36), the above provides an explicit expression for $\zeta^*(\Delta\varepsilon_q)$:

$$\sin\zeta^* = \frac{\sqrt{3/2}\,\Delta\varepsilon_q \tan\theta_{cr}}{\|\mathbf{s}^e\|/2G} = \frac{3G\Delta\varepsilon_q\ \tan\theta_{cr}}{q^e} \tag{41}$$

Equation (41) may be used to eliminate ζ^* from (35), yielding a scalar equation of the equivalent plastic strain increment $\Delta\varepsilon_q$:

$$F_{p2}(\Delta\varepsilon_q) = \left[\Delta\varepsilon_q + \frac{k_{n+1}(\Delta\varepsilon_q)}{3G}\right]^2 + \left[\Delta\varepsilon_q \tan\theta_{cr}\right]^2 - \left(\frac{q^e}{3G}\right)^2 = 0 \tag{42}$$

which can be solved numerically. For linear hardening, it reduces to a second-order polynomial of $\Delta\varepsilon_q$, with a single positive solution, which was obtained by Simo (1987). On obtainment of $\Delta\varepsilon_q$, all remaining parameters are updated and ultimately the plastic strain increment $\Delta\mathbf{e}^p$ and the new stress state $\boldsymbol{\sigma}_{n+1}$ are calculated using (27) and (22). In Figure 8 a qualitative comparison is made for the integration process using the classical associative model and the present model. For a given stress state $\mathbf{s}_n$ and non-proportional strain increment $\Delta\mathbf{e}$, the converged state of the associative model corresponds to the largest expansion of the yield surface, while the present model results to smaller expansion of the yield surface, denoting its comparatively less stiff behavior.

Table 5 Integration algorithm for three-dimensional element analysis

(1) Compute trial elastic stress (elastic prediction)

$$\boldsymbol{\sigma}^e = \boldsymbol{\sigma}_n + \mathbf{D}\Delta\boldsymbol{\varepsilon} \quad , \qquad \mathbf{s}^e = \mathbf{I}^{dev}\boldsymbol{\sigma}^e \quad , \qquad p^e = -1/3\,(\mathbf{I}\cdot\boldsymbol{\sigma}^e)$$

$$q^e = \sqrt{3/2}\,\|\mathbf{s}^e\|\,, \qquad k_n = k\big(\varepsilon_{q|n}\big), \qquad F_{n+1}^{trial} = \frac{1}{2G}\left[\|\mathbf{s}^e\| - \sqrt{2/3}\,k_n\right]$$

(2) IF $F_{n+1}^{trial} \le 0$ THEN

$$\Delta\mathbf{e}^p = \mathbf{0} \qquad , \qquad \Delta\varepsilon_q = 0$$

ELSE ($F_{n+1}^{trial} > 0$)

$$\mathbf{n}_n = \frac{\mathbf{s}_n}{\|\mathbf{s}_n\|} \qquad , \qquad \mathbf{m}_n = \frac{[\mathbf{I}^{dev} - \mathbf{n}_n \otimes \mathbf{n}_n]\,\Delta\mathbf{e}}{\|[\mathbf{I}^{dev} - \mathbf{n}_n \otimes \mathbf{n}_n]\,\Delta\mathbf{e}\,\|}$$

$$\cos\theta_n = \frac{\mathbf{n}_n \cdot \Delta\mathbf{e}}{\|\Delta\mathbf{e}\|}, \qquad \cos\theta^e = \frac{\Delta\mathbf{e}\cdot\,\mathbf{s}^e}{\|\Delta\mathbf{e}\|\|\mathbf{s}^e\|}, \qquad \cos\zeta^e = \frac{\mathbf{s}_n\cdot\,\mathbf{s}^e}{\|\mathbf{s}_n\|\|\mathbf{s}^e\|}$$

(2a) Assume 1st branch is activated

To calculate $\Delta\varepsilon_q$ solve:

$$F_{p1}\big(\Delta\varepsilon_q\big) = 1 + \tan^2\zeta^* - \left[\frac{q^e}{k_{n+1} + 3G\Delta\varepsilon_q}\right]^2$$

with

$$\zeta^*(\Delta\varepsilon_q) = \tan^{-1}\left[\frac{\sin\theta^e}{\frac{\|\mathbf{s}^e\|}{2G\|\Delta\mathbf{e}\|}\left[1 + \frac{h_{n+1}}{3G}\right] - \cos\theta^e}\right]$$

Compute:

$$\bar{h}_{n+1} = h_{n+1} \quad , \qquad \theta = \theta^e + \zeta^*$$

$$\theta^p = \tan^{-1}\left[\frac{\frac{\|\Delta\mathbf{e}\|\sin\theta}{1 + \bar{h}_{n+1}/3G}}{\sqrt{3/2}\,\Delta\varepsilon_q}\right]$$

(2b) If $\theta^p > \theta_{cr}$: the second branch is activated

To calculate $\Delta\varepsilon_q$ solve:

$$F_{p2}\big(\Delta\varepsilon_q\big) = \left[\Delta\varepsilon_q + \frac{k_{n+1}\big(\Delta\varepsilon_q\big)}{3G}\right]^2 + \big[\Delta\varepsilon_q \tan\theta_{cr}\big]^2 - \left(\frac{q^e}{3G}\right)^2 = 0$$

Compute:

$$\zeta^*\big(\Delta\varepsilon_q\big) = \sin^{-1}\left[\frac{3G\Delta\varepsilon_q\,\tan\theta_{cr}}{q^e}\right], \qquad \theta = \theta^e + \zeta^*, \qquad \theta^p = \theta_{cr}$$

$$\bar{h}_{n+1} = 3G\left(\frac{\|\Delta\mathbf{e}\|\sin\theta}{\sqrt{3/2}\,\Delta\varepsilon_q\tan\theta_{cr}} - 1\right)$$

(2c) Calculate the plastic strain increment

$$\zeta = \zeta^e - \zeta^*$$

$$\mathbf{n}_{n+1} = \quad \cos\zeta\,\mathbf{n}_n + \sin\zeta\,\mathbf{m}_n, \qquad \mathbf{m}_{n+1} = -\sin\zeta\,\mathbf{n}_n + \cos\zeta\,\mathbf{m}_n$$

$$\Delta\mathbf{e}^p = \sqrt{3/2}\,\Delta\varepsilon_q\,\mathbf{n}_{n+1} + \frac{\|\Delta\mathbf{e}\|\sin\theta}{1 + \bar{h}_{n+1}/3G}\,\mathbf{m}_{n+1}$$

(3) Update stress tensor and state variables

$$\boldsymbol{\sigma}_{n+1} = \boldsymbol{\sigma}^e - 2G\Delta\mathbf{e}^p$$

$$\varepsilon_{q|n+1} = \varepsilon_{q|n} + \Delta\varepsilon_q$$

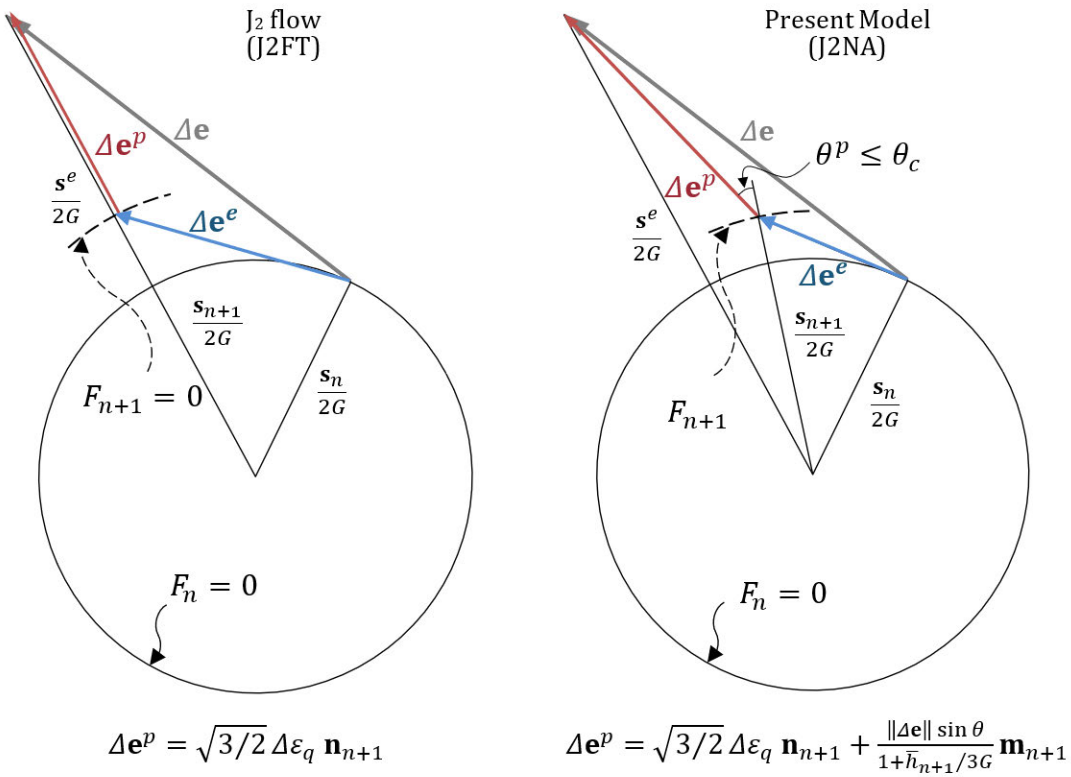

Figure 8 Representation of the stress update algorithm for a given strain increment employing the associative model and the present model.

3.4 Consistent algorithmic moduli

To maintain quadratic convergence of the finite element solution, the material stiffness moduli consistent with the integration scheme are obtained and used in the iterative solution. These, are computed from the fundamental equation (43) (Simo & Taylor, 1985). For convenience the volumetric and the deviatoric part of stress and strain are isolated:

$$\mathbf{D}_{ep}^{c} = \frac{\partial \boldsymbol{\sigma}_{n+1}}{\partial \boldsymbol{\varepsilon}_{n+1}} = 3K\,\mathbf{I}^{vol} + \frac{\partial \mathbf{s}_{n+1}}{\partial \mathbf{e}_{n+1}} \tag{43}$$

The fourth-order tensor $\partial \mathbf{s}_{n+1}/\partial \mathbf{e}_{n+1}$ is obtained for each model branch, by expressing the differential of the stress deviator as a function of the differential of the strain increment, accounting for the dependence of all internal variables to the strain increment. The stress deviator at the converged state is:

$$\mathbf{s}_{n+1}\left(\Delta\varepsilon_q, \zeta^*, \Delta\mathbf{e}\right) = \sqrt{2/3}\, k_{n+1}[\cos(\zeta^e - \zeta^*)\, \mathbf{n}_n + \sin(\zeta^e - \zeta^*)\, \mathbf{m}_n] \tag{44}$$

Therefore, differentiating using the chain rule, one obtains:

$$d\mathbf{s}_{n+1} = \frac{\partial \mathbf{s}_{n+1}}{\partial \mathbf{e}_{n+1}} d\Delta\mathbf{e} = \left[\mathbf{s}_{n+1,\Delta\varepsilon_q} \otimes \Delta\varepsilon_{q,\Delta\mathbf{e}} + \mathbf{s}_{n+1,\zeta^*} \otimes \zeta^*{}_{,\Delta\mathbf{e}} + \mathbf{s}_{n+1,\Delta\mathbf{e}}\right] d\Delta\mathbf{e} \tag{45}$$

where a $(\cdot)_{,x}$ implies partial derivative with respect to x. All referenced derivatives are offered in Appendix I. The terms $\Delta\varepsilon_{q,\Delta\mathbf{e}}$ and $\zeta^*_{,\Delta\mathbf{e}}$ are obtained from the differentials of the respective definition of the two internal variables, which generally take the form

$$F_1\left(\Delta\varepsilon_q, \zeta^*, \Delta\mathbf{e}\right) = 0 \tag{46}$$

$$F_2\left(\Delta\varepsilon_q, \zeta^*, \Delta\mathbf{e}\right) = 0 \tag{47}$$

The functions F_1, F_2 are characteristic to each model/model branch and are summarized in Table 6. From their differentials it follows:

$$\begin{bmatrix} \Delta\varepsilon_q{}_{,\Delta\mathbf{e}} \\ \zeta^*{}_{,\Delta\mathbf{e}} \end{bmatrix} = -\begin{bmatrix} F_{1,\Delta\varepsilon_q} & F_{1,\zeta^*} \\ F_{2,\Delta\varepsilon_q} & F_{2,\zeta^*} \end{bmatrix}^{-1} \begin{bmatrix} F_{1,\Delta\mathbf{e}} \\ F_{2,\Delta\mathbf{e}} \end{bmatrix} \tag{48}$$

Accounting for the direction angle dependence in the linearization is the key issue in obtaining the consistent moduli for this type of models, an issue not addressed in similar works. Finally, the tensor $\partial\mathbf{s}_{n+1}/\partial\mathbf{e}_{n+1}$ may be expressed in terms of $\mathbf{n}_{n+1}, \mathbf{m}_{n+1}$ as follows:

$$\begin{aligned} \frac{\partial \mathbf{s}_{n+1}}{\partial \mathbf{e}_{n+1}} = D^{dev}\mathbf{I}^{dev} + D^{nn}\,(\mathbf{n}_{n+1} \otimes \mathbf{n}_{n+1}) + D^{nm}\,(\mathbf{n}_{n+1} \otimes \mathbf{m}_{n+1}) \\ + D^{mn}\,(\mathbf{m}_{n+1} \otimes \mathbf{n}_{n+1}) + D^{mm}\,(\mathbf{m}_{n+1} \otimes \mathbf{m}_{n+1}) \end{aligned} \tag{49}$$

where

$$D^{dev} = \sqrt{2/3}\, k_{n+1} \frac{\sin\zeta}{\|\Delta\mathbf{e}\| \sin\theta_n}, \qquad B = \frac{2G\|\Delta\mathbf{e}\| \sin\theta_n}{\|\mathbf{s}^e\| \sin\zeta} \tag{50}$$

$$\begin{bmatrix} D^{nn} & D^{nm} \\ D^{mn} & D^{mm} \end{bmatrix} = D^{dev} \begin{bmatrix} -1 & 0 \\ -B\sin\zeta^* & -1 + B\cos\zeta^* \end{bmatrix} - \begin{bmatrix} \mathbf{s}^{\mathbf{n}}_{n+1,\Delta\varepsilon_q} & \mathbf{s}^{\mathbf{n}}_{n+1,\zeta^*} \\ \mathbf{s}^{\mathbf{m}}_{n+1,\Delta\varepsilon_q} & \mathbf{s}^{\mathbf{m}}_{n+1,\zeta^*} \end{bmatrix} \begin{bmatrix} F_{1,\Delta\varepsilon_q} & F_{1,\zeta^*} \\ F_{2,\Delta\varepsilon_q} & F_{2,\zeta^*} \end{bmatrix}^{-1} \begin{bmatrix} F^{\mathbf{n}}_{1,\Delta\mathbf{e}} & F^{\mathbf{m}}_{1,\Delta\mathbf{e}} \\ F^{\mathbf{n}}_{2,\Delta\mathbf{e}} & F^{\mathbf{m}}_{2,\Delta\mathbf{e}} \end{bmatrix} \tag{51}$$

In the above $\mathbf{F}_i^{\mathbf{n}} = \mathbf{n}_{n+1} \cdot \mathbf{F}_i$, and $\mathbf{F}_i^{\mathbf{m}} = \mathbf{m}_{n+1} \cdot \mathbf{F}_i$, are the components of tensor $\mathbf{F}$ in the directions of tensors $\mathbf{n}_{n+1}$ and $\mathbf{m}_{n+1}$.The linearized moduli are non-symmetric, as the multipliers D^{mn} and D^{nm} of the non-symmetric terms $\mathbf{m}_{n+1} \otimes \mathbf{n}_{n+1}$ and $\mathbf{n}_{n+1} \otimes \mathbf{m}_{n+1}$ respectively, are not equal. Thus, $D^c_{ep(ijkl)} \neq D^c_{ep(klij)}$, while the symmetries $D^c_{ep(ijkl)} = D^c_{ep(ijlk)} = D^c_{ep(jikl)} = D^c_{ep(jilk)}$ are preserved. In the limit $\|\Delta\mathbf{e}\| \to 0$, the linearized moduli reduce to the material tangent moduli.

Table 6 Functions necessary to define internal variables $\Delta\varepsilon_q$, ζ^*

model / branch	$F_1 = 0$	$F_2 = 0$
1st branch - $\bar{h} = k(\varepsilon_q)/\varepsilon_q$	Eq. (39)	Eq. (38)
2nd branch - $\theta^p = \theta_{cr}$	Eq. (42)	Eq. (41)
Explicit choice: $\bar{h} = \bar{h}(\theta, \Delta\varepsilon_q)$	Eq. (36)	Eq. (35)

3.5 Accuracy Analysis - Iso-error Maps

To test numerically the accuracy of the developed algorithm, iso-error maps are constructed for a material point under strain-controlled loading. The iso-error maps offer a schematic representation of the accuracy of the integration algorithm under a variety of loading paths. In the present study, the loading cases suggested by Simo & Taylor (1986) are used to test the accuracy of the developed non-associative model. The model is being tested for shell elements in plane stress loading conditions ($\sigma_{33} = \sigma_{13} = \sigma_{23} = 0$).

Starting from a stress state on the yield surface (points A,B,C in Figure 9), the new stress state $\boldsymbol{\sigma}(\Delta\boldsymbol{\varepsilon})$ is calculated for a range of strain increments (combinations of $\Delta\varepsilon_{11}$ and $\Delta\varepsilon_{22}$), employing the developed integration scheme. Subsequently, each strain increment $\Delta\boldsymbol{\varepsilon}$ is divided in increasingly smaller sub-increments and employing the developed integration scheme for each sub increment,

the 'exact' solution $\boldsymbol{\sigma}^*$ is obtained. The number of sub-increments is increased until convergence of $\boldsymbol{\sigma}^*$. The error of the integration is estimated according to the expression:

$$e(\%) = 100 \cdot \|\mathbf{s} - \mathbf{s}^*\| / \|\mathbf{s}^*\| \tag{52}$$

Three initial stress states are considered: (A) uniaxial, (B) biaxial and (C) pure shear loading, which represent a wide range of initial loading conditions. The strain increments are normalized with the yield strain parameter $\varepsilon_y = \sigma_y/E = 0.1\%$. In all iso-error maps the shear stress is taken as zero ($\sigma_{12} = 0$). The unfavorable case of rigid plasticity is considered, with the material properties in Table 7

Table 7 Material properties and state variables for Iso-Error Maps

Poisson's Ratio	$\nu = 0.3$
Young's Modulus	$E = 207\ GPa\ (30000\ ksi)$
Von Mises Stress	$\sigma_y = 207\ MPa(\ 30\ ksi)$
Hardening modulus	$H = 0\ GPa$

The level of error for this model is similar to that reported previously in the literature and the J2FT, which is up to 8% for strain increments of the size of the yield strain. Increasing the hardening modulus leads to somewhat smaller error, because the denominator of equation (52) that expresses the size of the yield surface increases. The algorithm exhibits no error for the case of proportional loading, namely, along the line $\Delta\varepsilon_{22}/\ \Delta\varepsilon_{11} = 0.5$ in Figure 9(A), and lines $\Delta\varepsilon_{22}/\Delta\varepsilon_{11} = 1,$ in Figure 9(B, C).

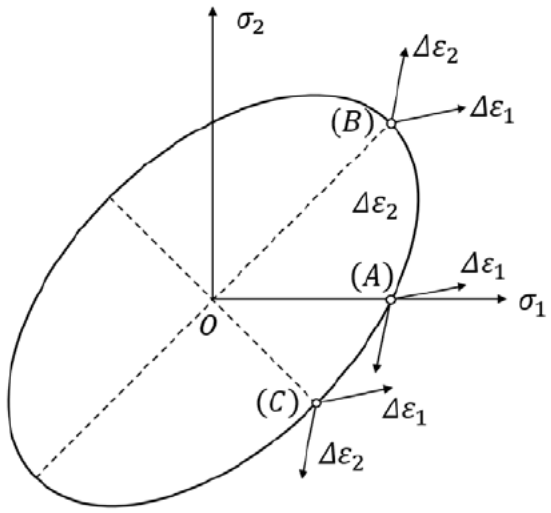

(0) Plane stress yield surface, points A, B, C

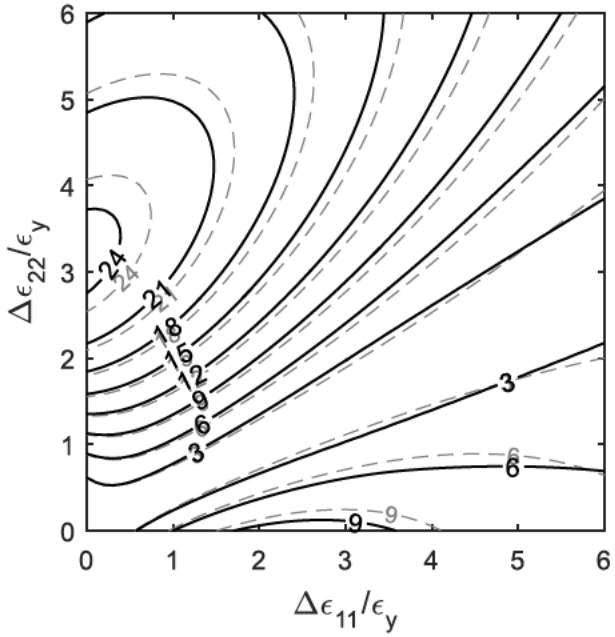

(A) Point A – Uniaxial loading initial state

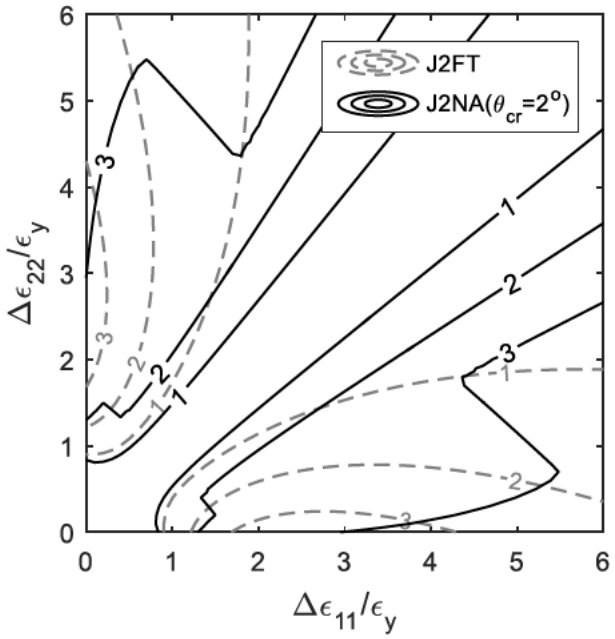

(B) Point B – Biaxial loading initial state

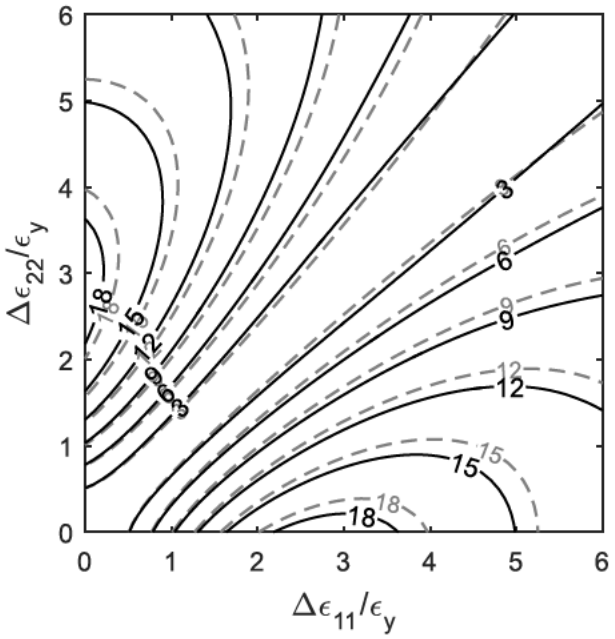

(C) Point C – Pure Shear initial state

Figure 9 Isoerror maps for different points A, B and C on the yield surface.

4 Shell buckling calculations

4.1 Implementation in a finite element environment

Lower bound estimates of the bifurcation load from the pre-buckling equilibrium path can be obtained using Hill's 'comparison solid' concept. Hutchinson (1974) described in detail its implementation and Tvergaard (1983a) discussed its application using the J_2 corner theory proposed by Christoffersen and Hutchinson (1979), which employs material moduli dependent on the direction of the strain rate. The comparison solid concept introduces a quadratic functional, based on the virtual work principle, whose positiveness ensures stability, while the occurrence of non-positive values indicates bifurcation:

$$F = \mathbf{\Delta U}^T \ [\mathbf{K}'] \ \mathbf{\Delta U} \tag{53}$$

In the above, $[\mathbf{K}']$ is the global stiffness matrix that employs the tangent material moduli of the constitutive model, and $\mathbf{\Delta U}$ is the vector with the unconstrained degrees of freedom. The elastoplastic tangent moduli are used for material points whose loading state is on the surface of their respective yield surfaces and the elastic moduli in all other cases. This expression implies that instability occurs when a non-positive eigenvalue of $[\mathbf{K}']$ is encountered.

Using the implicit finite element environment in ABAQUS/Standard, the global stiffness matrix $[\mathbf{K}']$ can be extracted using a dedicated step and a material subroutine UMAT to apply the material elastoplastic tangent moduli. Eliminating the constrained degrees of freedom, the eigenvalues may be calculated externally, and bifurcation is identified at the first zero eigenvalue. Alternatively, using a linear perturbation step, the smallest eigenvalues and the respective eigenmodes can be obtained to detect bifurcation. In a static analysis, by default, ABAQUS identifies and records the occurrence of non-positive eigenvalues of the stiffness matrix, which is an alternative way of identifying bifurcation. Implicit analyses, however, employ the algorithmic moduli of the constitutive models in

their calculations, which differ from the tangent moduli. Therefore, they may lead to non-accurate bifurcation estimates, especially when large strain increments are used. Nonetheless, in all cases analyzed in the present study, the above methods yielded the same bifurcation estimates.

For non-associative models, the material tangent moduli depend on the direction (angle θ) of the subsequent strain increment at each material point, which is not known. Hence, the instantaneous moduli associated with the angle θ of the previous strain increment are used, assuming an 'alternative comparison solid', a concept introduced by Tvergaard (1983a).

4.2 Numerical results

4.2.1 Axisymmetric buckling of axially compressed tubes

The plastic buckling of thick-walled metal cylindrical shells under compression is briefly addressed to demonstrate the key features and capabilities of the developed framework. The pre-buckling path is characterized by proportional loading well into the plastic range of the material, until bifurcation into an axisymmetric buckling mode occurs, associated with the development of wrinkles, uniform along the cylinder (Gellin, 1979). The critical bifurcation stress (σ_c) and the corresponding half-wave length (λ_c), can be calculated analytically using the equations:

$$\sigma_c = \left[\frac{D_{11}D_{22} - D_{12}^2}{3}\right]^{1/2} \left(\frac{t}{R}\right) \tag{54}$$

$$\frac{\lambda_c}{R} = \left[\frac{D_{11}^2}{12(D_{11}D_{22} - D_{11}^2)}\right]^{1/4} \left(\frac{t}{R}\right)^{1/2} \tag{55}$$

where R is the radius of the tube, t is its thickness and $D_{\alpha\beta} = \partial\sigma_{\alpha\beta}/\partial\varepsilon_{\alpha\beta}$ (no summation on α, β) is the condensed material stiffness tensor $D_{ep\,(\alpha\beta\alpha\beta)}^{c.shell}, \alpha, \beta = 1{,}2$ presented in equation (II.3). In the

absence of initial geometric imperfection, the pre-buckling average stress-shortening response follows the material compression curve independently of the material model, while the use of different material stiffness moduli may provide significantly different bifurcation estimates. Key features of the presented methodology are demonstrated below in simulating numerically buckling of thick-walled duplex stainless steel tubes reported in (Bardi & Kyriakides, 2006; Bardi et al., 2006). Those experiments were designed to mitigate the influence of edge supports and represent the bifurcation behavior of long shells, as opposed to older investigations on axially-compressed cylinders (Lee, 1962; Batterman, 1965), where specimen length and support conditions prevented the clear identification of wrinkling onset, which may result in misleading comparisons between bifurcation and collapse loads.

In Figure 10 (b,c,d), the axisymmetric bifurcation stress (σ_c), strain (ε_c) and the corresponding half-wave length (λ_c) are displayed for tubes in terms of the diameter-to-thickness ratio (D/t). Bifurcation from the pre-buckling path is identified by solving expression (54) employing the material moduli for different constitutive models. The predictions for J2NA and J2DT are identical as the preloading is proportional leading to the same material moduli. The J2FT over-predicts by a significant amount the bifurcation stresses in the entire range considered, while J2NA provides predictions in better agreement in general. On the other hand, the non-associative model by Simo (1987) predicts bifurcation at significantly lower load than experiments indicate. The differences are more salient when the values of strain at bifurcation are considered in Figure 10(c). In that case, the J2FT grossly over-predicts bifurcation strains, whereas the present model is in better agreement with experiments. Finally, the model by Simo leads to significant underpredictions of the bifurcation strain, especially for larger values of D/t ratio. Experimental values by (Bardi & Kyriakides, 2006) are marked with circles and squares.

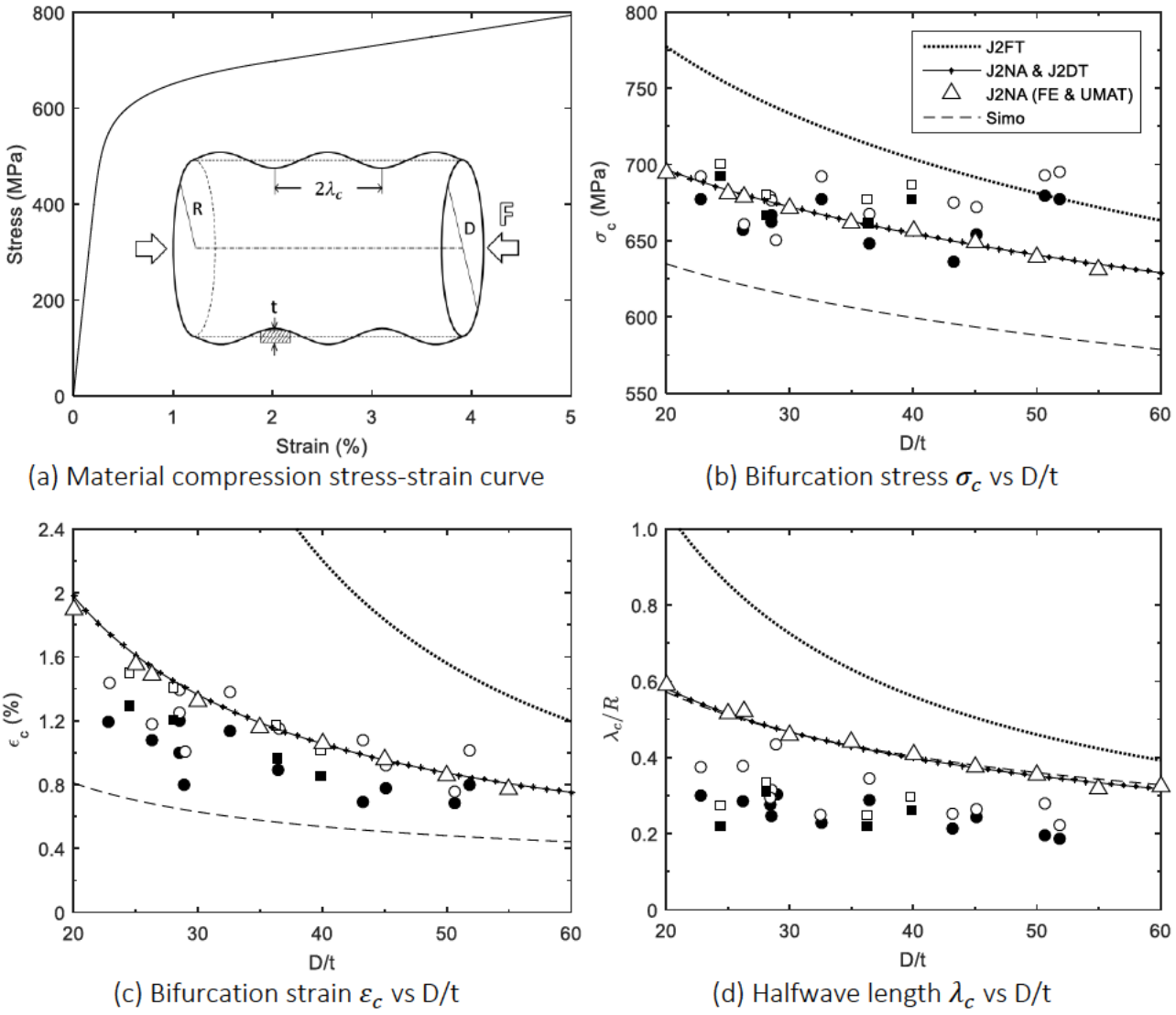

(a) Material compression stress-strain curve

(b) Bifurcation stress σ_c vs D/t

(c) Bifurcation strain ε_c vs D/t

(d) Halfwave length λ_c vs D/t

Figure 10 Material curve and bifurcation stress, bifurcation parameters obtained employing different plasticity constitutive laws. Experimental data are included

The buckling half-wave length is overestimated by all models. Simo's model yields predictions similar to the ones by J2NA, which are more consistent with experimental results compared to those of J2FT, but still over-predict the reported half-wave values by a factor of 2. The differences can be alleviated when yield anisotropy is taken accounted for (Bardi & Kyriakides, 2006; Corona et al., 2006; Kyriakides et al., 2005), but this is outside the scope of the present study.

Bifurcation predictions were also obtained using finite element models via static analyses in ABAQUS, employing the user-material-subroutine (UMAT) for J2NA. Axisymmetric and three-dimensional shell models with different lengths were used, under a displacement-controlled analysis scheme. A series of analyses was performed to identify the earliest bifurcation and the length for which it occurs, which provided the three bifurcation parameters. The finite element results are included with triangular marks in Figure 10(b,c,d), and they are in very good agreement with the analytical predictions.

4.2.2 Non-axisymmetric buckling modes

To investigate the development of non-axisymmetric bifurcation modes, models of length $L = 2\kappa\lambda_{HW}$ (κ is an integer) are used, following the argument by (Gellin, 1979). Models employ 12 S4 elements per halfwave and 120 in the circumference, together with periodic symmetry support conditions. Shortening is imposed incrementally and at 0.1% strain increment, the eigenvalues of the stiffness matrix are monitored. The first zero eigenvalues represent an axisymmetric buckling mode and occur at stress, strain, and wavelength in agreement with the analytical solution. At increasing deformations, bifurcation into non-symmetric modes with two and tree circumferential waves was also recorded.

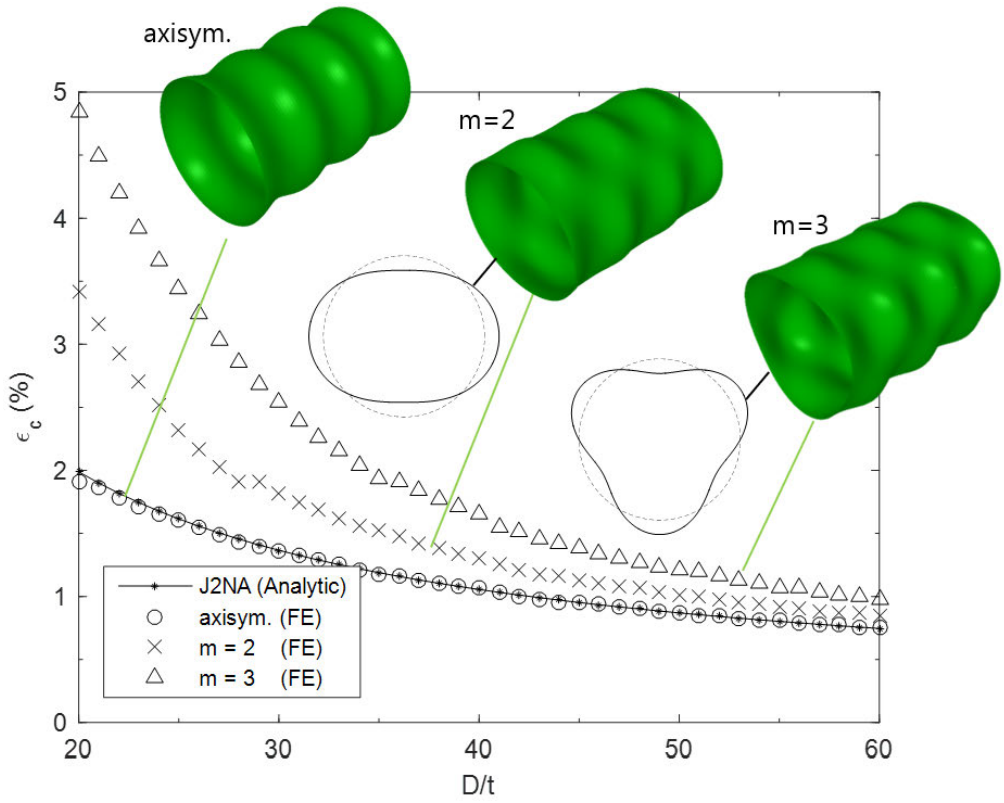

Figure 11 Bifurcation to non-axisymmetric bucking modes employing J2NA

4.2.3 Wrinkling evolution and localization

Initial geometric imperfection leads to non-uniform stress distribution along the tube and non-proportionality arises, which surfaces the differences between the constitutive models. A demonstration of these differences is made by comparing the average stress (F/A) - normalized shortening ($\Delta L/L$) diagrams of initially uniformly-wrinkled tubes under compression (Figures 12-14).

Displacement-controlled axisymmetric analyses were performed, employing 20 two-node axisymmetric shell elements, denoted as SAX1 in ABAQUS, simulating one half-wave length of the cylinder. Imperfection in the shape of the first (axisymmetric) eigenmode is included with amplitude ωt, where parameter ω refers to the amplitude of the imperfection as a percentage of the shell thickness. The behavior of the imperfect cylinder is presented in Figure 12, using the present model with angle values θ_{cr} equal to $2°, 5°, 10°, 15°, 30°$, as well as the J2FT and J2DT models for

comparison purposes. A small imperfection parameter $\omega = 10^{-4}$ is used, which enables the solution to follow the secondary path, without an abrupt transition at the bifurcation point.

The J2FT follows the primary path, which is practically the material curve under compression for axial shortening up to 5% average strain, and develops a load maximum at about 6% average strain. On the contrary, the J2DT model develops a load maximum at the bifurcation point of the perfect system, followed by a decreasing branch. The behavior of the present non-associative model (J2NA) is bounded by these two models. At bifurcation, the cylinder starts diverging from the primary path with increasing load. The parameter θ_{cr} influences the load maximum which the tube exhibits, with larger values of θ_{cr} leading to lower load maxima. As the angle θ_{cr} becomes very small, the present model response approaches that of the associative model. It is important to notice that a small value of angle θ_{cr} e.g. $2°$, can lead to a response which is quite different from that of J2FT (Figure 12).

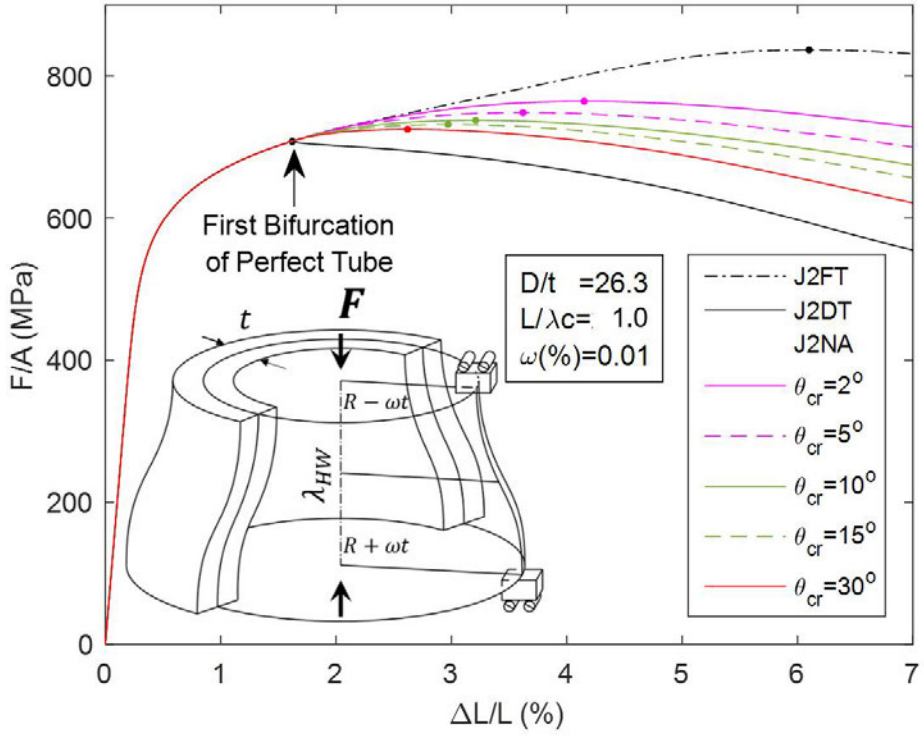

Figure 12 Effect of different constitutive models and model parameters in compressed tubes with small imperfection amplitude.

In Figure 13, when using the J2FT with a very small value of initial geometric imperfection (parameter $\omega = 10^{-5}$), no maximum load is identified for average shortening up to 7%. On the other hand, using the J2NA with $\theta_{cr} = 2^{o}$ and the same initial imperfection profile, the tube's response follows a secondary equilibrium path, leading to a limit load at shortening $\Delta L/L = 4.5\%$. The values of angle θ in the neighborhood of 2% strain exceed 40°, indicating significant non-proportionality on the loading path. Similarly, considering imperfection levels $\omega \leq 0.01\%$ this behavior remains practically unaffected. For larger values of imperfection parameter $\omega > 0.1\%$ the equilibrium paths calculated using the two constitutive laws (J2FT and J2NA) become increasingly similar, while they are almost identical for $\omega = 10\%$.

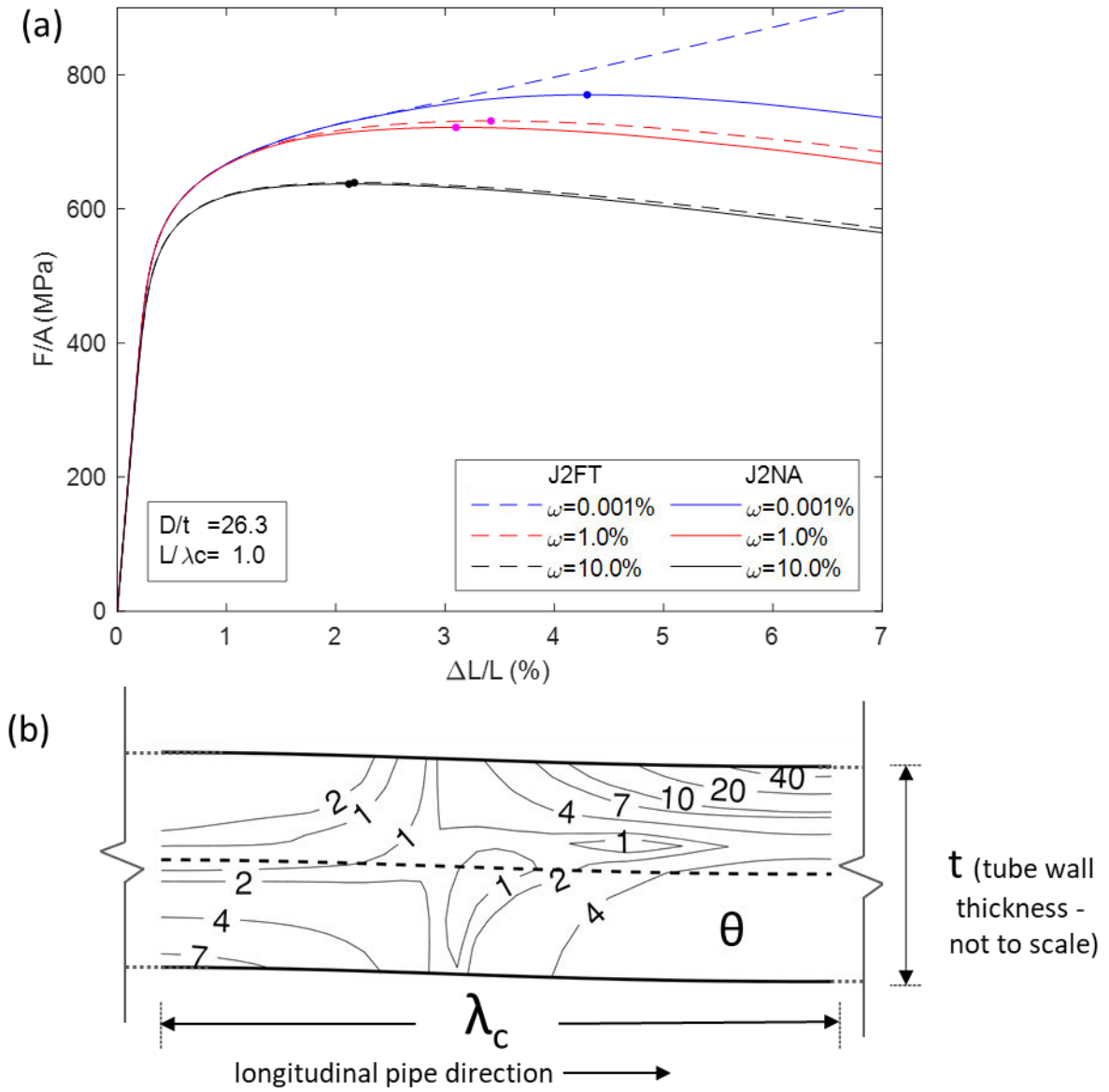

Figure 13 (a)Effect of imperfection amplitude on uniform wrinkling, using the J_2 flow and the non-associative model $\boldsymbol{\theta_{cr} = 2°}$; (b) angle $\boldsymbol{\theta}$ along a wavelength at $\boldsymbol{\varepsilon = 2\%}$, $\boldsymbol{\omega = 10^{-5}}$

Similar behavior was found in the localization of wrinkling in 14-halfwave-long models with the same mesh density (Figure 14). The tube is found to maintain rigidity up until greater deformations when employing the J2FT. For both constitutive models, wrinkling was found to localize in an outward buckle, which is in agreement with observations by Tvergaard (1983a). In Figure 14 the increase in diameter along the tube is further given for different stages of the analysis, as well as the strain direction angle θ in an advanced stage of the post-buckling ($\Delta L/L = 6\%$). Great variations are seen in θ, and values greater than 90^o in unloading parts of the tube.

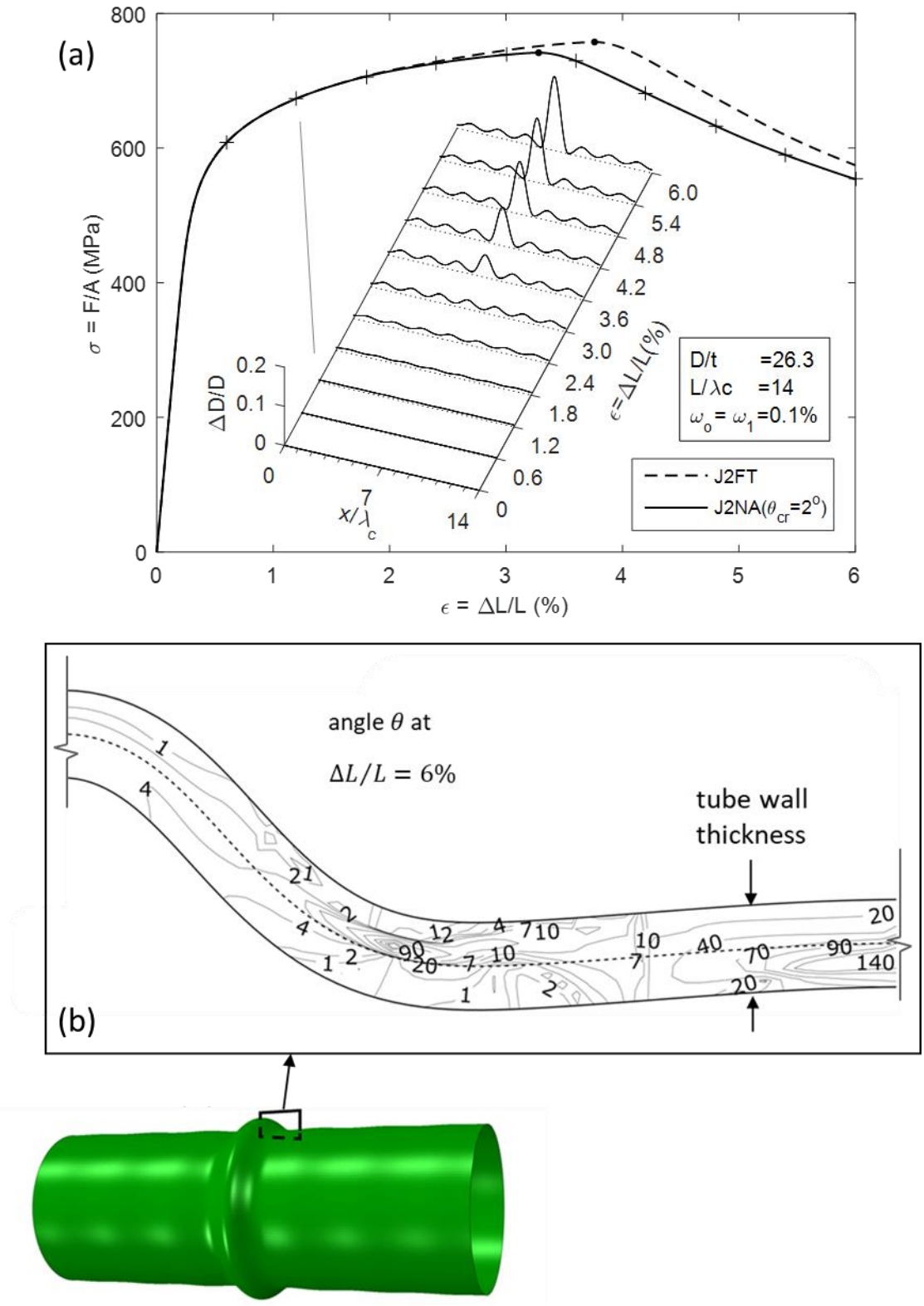

Figure 14 (a)Post-buckling and deformation localization in the compressed shell; change in diameter along the tube segment at different strains; (b) strain direction angle $\boldsymbol{\theta}$ in the post-buckling.

Conclusions

A constitutive model has been developed and implemented for simulating the structural behavior of thick-walled metal shells under compressive loading, focusing on their structural instability and post-buckling response. The model assumes a Von Mises yield surface and a non-associative flow rule, dependent on the direction of the strain rates. Fully elastic unloading is implemented for strain rates directed tangent to or inwards the yield surface. Care is taken to eliminate any discontinuity in the plastic strain production for strain rate directions near the yield surface tangent, by adopting a strain-direction-dependent non-associative hardening parameter $\bar{h}$, which moderates the production of plastic strain. Upon proper selection of $\bar{h}$, the model's formulation can represent several pseudo-corner models proposed elsewhere, which allow for different amounts of production of plastic strain.

A two-branch flow rule is presented for buckling of thick-walled shells: for small deviations from proportional loading, it employs the rate form of the J_2 deformation theory to inherit its effectiveness in estimating bifurcation. For larger deviations from proportional loading, the flow mimics the effect of a corner in the yield surface, constraining the plastic strain increment to be directed within this 'vertex'. The non-associative hardening parameter $\bar{h}$ is used to implement the model's pseudo-corner-effect and enable a smooth transition to elastic unloading.

A robust and efficient integration algorithm is developed for the constitutive model using a backward-Euler scheme for three-dimensional solid elements, together with an enhanced version for shell element analysis. In both cases the consistent algorithmic moduli are derived. The present model is capable of representing more compliant mechanical behavior than the J_2 flow model by adopting the beneficial aspects of J_2 deformation theory, while overcoming the latter's shortcomings in unloading.

The model is implemented in a finite-element environment as a material user subroutine, and it is used for predicting the structural response and instability of thick-walled metal cylindrical shells

under axial compression. Bifurcation estimates are obtained for axisymmetric and non-axisymmetric modes, and good agreement is found with available experimental data, while the non-associative flow by Simo (1987) produces unrealistically low bifurcation predictions for axially-compressed cylinders. Furthermore, the present model is capable of simulating the post-buckling behavior of axially compressed shells, which is characterized by significantly non-proportional strain paths.

The constitutive model accounts for different amounts of non-associative straining in the context of pseudo-corner plasticity, and its numerical implementation offers a framework for implementing efficiently pseudo-corner plasticity models in a finite element environment. The developed numerical approach can be used as an effective tool for performing numerical calculations in shell instability problems and is capable of predicting the maximum load, the corresponding deformation, and the post-buckling behavior, in good agreement with available experimental data.

Acknowledgements

The present work was supported by a Ph.D. studentship offered to the first author from the School of Engineering, The University of Edinburgh, Scotland, UK.

Appendix I - Details of numerical implementation

According to (44), the deviatoric stress tensor at the converged state is expressed as:

$$\begin{aligned}\mathbf{s}_{n+1}\left(\Delta\varepsilon_q, \zeta^*, \Delta\mathbf{e}\right) &= \sqrt{2/3}\, k_{n+1}\, \mathbf{n}_{n+1} \\ &= \sqrt{2/3}\, k_{n+1}\left(\Delta\varepsilon_q\right) \left[\cos(\zeta^e(\Delta\mathbf{e}) - \zeta^*)\, \mathbf{n}_n + \sin(\zeta^e(\Delta\mathbf{e}) - \zeta^*)\, \mathbf{m}_n(\Delta\mathbf{e})\right]\end{aligned} \tag{I.1}$$

From equation (I.1), the following derivatives are obtained, which are used in the calculation of linearized moduli:

$$\mathbf{s}_{n+1,\Delta\varepsilon_q} = \sqrt{2/3}\, H_{n+1}\, \mathbf{n}_{n+1} \tag{I.2}$$

$$\mathbf{s}_{n+1,\zeta^*} = -\sqrt{2/3}\, k_{n+1}\mathbf{m}_{n+1} \tag{I.3}$$

$$\mathbf{s}_{n+1,\Delta\mathbf{e}} = \sqrt{2/3}\, k_{n+1}\left[\mathbf{m}_{n+1} \otimes \frac{\partial\zeta^e}{\partial\Delta\mathbf{e}} + \sin(\zeta^e - \zeta^*)\frac{\partial\mathbf{m}_n}{\partial\Delta\mathbf{e}}\right] \tag{I.4}$$

where

$$\zeta^e_{,\Delta\mathbf{e}} = \frac{2G}{\|\mathbf{s}^e\|}\left[-\sin\zeta^e\, \mathbf{n}_n + \cos\zeta^e\, \mathbf{m}_n\right] \tag{I.5}$$

$$\frac{\partial\mathbf{m}_n}{\partial\Delta\mathbf{e}} = \frac{1}{\|\Delta\mathbf{e}\|\sin\theta_n}\left[\mathbf{I}^{dev} - \mathbf{n}_n \otimes \mathbf{n}_n - \mathbf{m}_n \otimes \mathbf{m}_n\right] \tag{I.6}$$

Equations (I.5) and (I.6) are obtained by differentiating the definitions in equations (34) and (28) respectively. Additionally, since $\theta^e = \theta_n - \zeta^e$, the following expressions can be derived:

$$\theta^e_{,\Delta\mathbf{e}} = \frac{1}{\|\Delta\mathbf{e}\|}\left[-\sin\theta_n\, \mathbf{n}_n + \cos\theta_n\, \mathbf{m}_n\right] - \frac{2G}{\|\mathbf{s}^e\|}\left[-\sin\zeta^e\, \mathbf{n}_n + \cos\zeta^e\, \mathbf{m}_n\right] \tag{I.7}$$

Expressions (I.1-I.7) are applicable for the integration algorithm and its linearization, irrespective of the definition of $\bar{h}$, and refer to both three-dimensional and shell elements.

I.1 First branch of the model ($\boldsymbol{\theta^p \le \theta_{cr}}$)

For the first branch of the model, the algorithm reduces to the system of equations (I.8) and (I.9), which is solved numerically, employing a local Newton scheme.

$$F_1(\Delta\varepsilon_q, \zeta^*, \Delta\mathbf{e}) = F_{p1} = 1 + \tan^2\zeta^* - \left[\frac{q^e}{k_{n+1} + 3G\Delta\varepsilon_q}\right]^2 = 0 \tag{I.8}$$

$$F_2(\Delta\varepsilon_q, \zeta^*, \Delta\mathbf{e}) = \tan\zeta^* - \frac{\tan\theta^e}{c-1} = 0 \tag{I.9}$$

where

$$c = \frac{\|\mathbf{s}^e\|}{2G\|\Delta\mathbf{e}\|\cos\theta^e}\left[1 + \frac{h_{n+1}}{3G}\right] = \frac{\mathbf{s}^e \cdot \mathbf{s}^e}{2G\Delta\mathbf{e} \cdot \mathbf{s}^e}\left[1 + \frac{h_{n+1}}{3G}\right] \tag{I.10}$$

The derivatives, used in the Newton scheme are:

$$F_{p1,_{\Delta\varepsilon_q}} = 2\left[\frac{q^e}{k_{n+1} + 3G\Delta\varepsilon_q}\right]^2 \frac{H_{n+1} + 3G}{k_{n+1} + 3G\Delta\varepsilon_q} \tag{I.11}$$

$$F_{p1,\zeta^*} = 2\tan\zeta^*\,(1 + \tan^2\zeta^*) \tag{I.12}$$

$$F_{p1,_{\Delta\mathbf{e}}} = -2\frac{3G\,\mathbf{s}^e}{\left[k_{n+1} + 3G\Delta\varepsilon_q\right]^2} \tag{I.13}$$

$$F_{2,_{\Delta\varepsilon_q}} = \frac{\tan\theta^e}{(c-1)^2}\,\frac{\|\mathbf{s}^e\|}{2G\|\Delta\mathbf{e}\|\cos\theta^e}\frac{\partial h_{n+1}/\partial\Delta\varepsilon_q}{3G} \tag{I.14}$$

$$F_{2,_{\zeta^*}} = 1 + \tan^2\zeta^* \tag{I.15}$$

$$\begin{aligned} F_{2,_{\Delta\mathbf{e}}} = &-\frac{1 + \tan^2\theta^e}{c-1}\theta^e_{,_{\Delta\mathbf{e}}} \\ &+ \frac{\tan\theta^e}{(c-1)^2}\,\frac{1}{\|\Delta\mathbf{e}\|\cos\theta^e}\left[2\frac{\mathbf{s}^e}{\|\mathbf{s}^e\|} - \frac{\|\mathbf{s}^e\|}{\|\Delta\mathbf{e}\|\cos\theta^e}\left[\frac{\mathbf{s}^e}{2G} + \Delta\mathbf{e}\right]\right]\left[1 + \frac{h_{n+1}}{3G}\right] \end{aligned} \tag{I.16}$$

Those derivatives are also employed in the linearization of the model.

Alternatively, as equation (I.9) offers an explicit expression for ζ^*, it can be used to eliminate it from (I.8), leading to :

$$\bar{F}_{p1}\big(\Delta\varepsilon_q, \Delta\mathbf{e}\big) = F_{p1}\big(\Delta\varepsilon_q, \zeta^*\big(\Delta\varepsilon_q, \Delta\mathbf{e}\big), \Delta\mathbf{e}\big) = \tag{I.17}$$

$$1+\left[\frac{\sin\theta^e}{\frac{\|\mathbf{s}^e\|}{2G\|\Delta\mathbf{e}\|}\left[1+\frac{h_{n+1}}{3G}\right]-\cos\theta^e}\right]^2-\left[\frac{q^e}{k_{n+1}+3G\Delta\varepsilon_q}\right]^2$$

For the three-dimensional formulation, equation (I.17) can be solved for $\Delta\varepsilon_q$ which is next substituted into (I.9) to provide ζ^*. Therefore, single variable equations need to be solved to define each of the unknowns. The derivatives used in this alternative expression of the problem and the subsequent linearization are:

$$\bar{F}_{p1,\Delta\varepsilon_q}=F_{p1,\Delta\varepsilon_q}+F_{p1,\zeta^*}\zeta^*_{,\Delta\varepsilon_q}=F_{p1,\Delta\varepsilon_q}+F_{p1,\zeta^*}\left(-\frac{F_{p2,\Delta\varepsilon_q}}{F_{p2,\zeta^*}}\right) \tag{I.18}$$

$$\bar{F}_{p1,\zeta^*}=0 \tag{I.19}$$

$$\bar{F}_{p1,\Delta\mathbf{e}}=F_{p1,\Delta\mathbf{e}}+F_{p1,\zeta^*}\zeta^*_{,\Delta\mathbf{e}}=F_{p1,\Delta\mathbf{e}}+F_{p1,\zeta^*}\left(-\frac{F_{p2,\Delta\mathbf{e}}}{F_{p2,\zeta^*}}\right) \tag{I.20}$$

Remark: Either version: $F_1=F_{p1}$ or $F_1=\bar{F}_{p1}$ can be used in solving for $\Delta\varepsilon_q$, ζ^* and either may be used in the subsequent linearization of the model, leading to identical results.

I.2 Second branch of the model ($\boldsymbol{\theta^p=\theta_{cr}}$)

For the second branch of the present model, equations (I.21) and (I.22) are solved numerically.

$$F_1=F_{p2}(\Delta\varepsilon_q,\Delta\mathbf{e})=\left[\Delta\varepsilon_q+\frac{k_{n+1}}{3G}\right]^2+\left[\Delta\varepsilon_q\tan\theta_{cr}\right]^2-\left(\frac{q^e}{3G}\right)^2=0 \tag{I.21}$$

$$F_2=\sin\zeta^*-\frac{3G\Delta\varepsilon_q\tan\theta_{cr}}{q^e}=0 \tag{I.22}$$

Using only (I.21), the equivalent plastic strain increment $\Delta\varepsilon_q$ can be obtained directly. Subsequently, (I.22) may then be solved to find ζ^*. The derivatives necessary for the solution of the two equations, also used in the consistent linearization, are:

$$F_{p2,\Delta\varepsilon_q} = 2\left[\Delta\varepsilon_q + \frac{k_{n+1}}{3G}\right]\left[1 + \frac{H_{n+1}}{3G}\right] + 2\Delta\varepsilon_q \tan^2\theta_{cr} \tag{I.23}$$

$$F_{p2,\zeta^*} = 0 \tag{I.24}$$

$$F_{p2,\Delta\mathbf{e}} = -6G\,\mathbf{s}^e/(3G)^2 \tag{I.25}$$

and

$$F_{2,\Delta\varepsilon_q} = -\frac{3G\tan\theta_{cr}}{q^e} \tag{I.26}$$

$$F_{2,\zeta^*} = \cos\zeta^* \tag{I.27}$$

$$F_{2,\Delta\mathbf{e}} = -\frac{3G\Delta\varepsilon_q\tan\theta_{cr}}{q^e}\,\frac{3G\boldsymbol{s}^e}{(q^e)^2} \tag{I.28}$$

I.3 Explicit definition of $\bar{\boldsymbol{h}}(\boldsymbol{\Delta\varepsilon_q}, \boldsymbol{\theta})$

A similar methodology can be applied in the case where a function $\bar{h}(\Delta\varepsilon_q, \theta)$ is defined explicitly. Adopting such an approach, the model by Pappa & Karamanos (2016) could be integrated and linearized, with $\bar{h}$ defined as reported Table 2. The system of equations (I.29) and (I.30) can be solved in terms of $(\Delta\varepsilon_q, \zeta^*)$ with $\theta = \theta^e + \zeta^*$, and it can be written as follows:

$$F_{p\bar{h}}(\Delta\varepsilon_q, \zeta^*, \Delta\mathbf{e}) = q^e\cos\zeta^* - \left[k_{n+1} + 3G\Delta\varepsilon_q\right] = 0 \tag{I.29}$$

$$L_{p\bar{h}}(\Delta\varepsilon_q, \zeta^*, \Delta\mathbf{e}) = q^e\sin\zeta^* - \sqrt{2/3}\,\frac{3G\|\Delta\mathbf{e}\|\sin(\theta^e + \zeta^*)}{1 + \bar{h}_{n+1}/3G} = 0 \tag{I.30}$$

with

$$\bar{h}_{n+1} = \bar{h}_{n+1}(\Delta\varepsilon_q, \theta = \theta^e + \zeta^*) \tag{I.31}$$

The derivatives used in the integration and the linearized moduli of the model are:

$$F_{p\bar{h},\Delta\varepsilon_q} = -[H_{n+1} + 3G] \tag{I.32}$$

$$F_{p\bar{h},\zeta^*} = -q^e\sin\zeta^* \tag{I.33}$$

$$F_{p\bar{h},\Delta\mathbf{e}} = \frac{3G\mathbf{s}^e}{q^e}\cos\zeta^* \tag{I.34}$$

and

$$L_{p\bar{h},\Delta\varepsilon_q} = +\sqrt{2/3}\frac{3G\|\Delta\mathbf{e}\|\sin(\theta^e+\zeta^*)}{\left[1+\bar{h}_{n+1}/3G\right]^2}\frac{\bar{h}_{n+1,\Delta\varepsilon_q}}{3G} \tag{I.35}$$

$$\begin{aligned} L_{p\bar{h},\zeta^*} &= q^e\cos\zeta^* \\ &\quad -\left[\sqrt{2/3}\frac{3G\|\Delta\mathbf{e}\|\cos(\theta^e+\zeta^*)}{1+\bar{h}_{n+1}/3G} - \sqrt{2/3}\frac{3G\|\Delta\mathbf{e}\|\sin(\theta^e+\zeta^*)}{\left[1+\bar{h}_{n+1}/3G\right]^2}\frac{\bar{h}_{n+1,\theta}}{3G}\right] \end{aligned} \tag{I.36}$$

$$\begin{aligned} L_{p\bar{h},\Delta\mathbf{e}} &= \frac{3G\mathbf{s}^e}{q^e}\sin\zeta^* \\ &\quad -\left[\sqrt{2/3}\frac{3G\sin(\theta^e+\zeta^*)}{1+\bar{h}_{n+1}/3G} - \sqrt{2/3}\frac{3G\|\Delta\mathbf{e}\|\sin(\theta^e+\zeta^*)}{\left[1+\bar{h}_{n+1}/3G\right]^2}\frac{\bar{h}_{n+1,\|\Delta\mathbf{e}\|}}{3G}\right]\frac{\Delta\mathbf{e}}{\|\Delta\mathbf{e}\|} \\ &\quad -\left[\sqrt{2/3}\frac{3G\|\Delta\mathbf{e}\|\cos(\theta^e+\zeta^*)}{1+\bar{h}_{n+1}/3G} - \sqrt{2/3}\frac{3G\|\Delta\mathbf{e}\|\sin(\theta^e+\zeta^*)}{\left[1+\bar{h}_{n+1}/3G\right]^2}\frac{\bar{h}_{n+1,\theta}}{3G}\right]\theta^e_{,\Delta\mathbf{e}} \end{aligned} \tag{I.37}$$

Appendix II- Algorithm for shell element analysis

In shell element analysis, for a given strain increment $\Delta\bar{\boldsymbol{\varepsilon}}$ (which has no $\Delta\varepsilon_{33}$ component), the stress at the converged state $\bar{\boldsymbol{\sigma}}_{n+1}$ (which has no $\bar{\sigma}_{n+1(33)}$ component) must be calculated, accounting for the traction component perpendicular to the shell lamina (assumed to be direction $\hat{\boldsymbol{e}}_3$) to vanish throughout the analysis:

$$\sigma_{n+1(33)} = 0 \tag{II.1}$$

The strain increment $\Delta\boldsymbol{\varepsilon}$ is decomposed as $\Delta\boldsymbol{\varepsilon} = \Delta\bar{\boldsymbol{\varepsilon}} + \Delta\varepsilon_{33}\mathbf{a}$, where $\Delta\varepsilon_{33}$ is the unknown component of the strain increment component perpendicular to the shell lamina, and $\mathbf{a} = \hat{\boldsymbol{e}}_3 \otimes \hat{\boldsymbol{e}}_3$

The constraint (II.1) is used to calculate $\Delta\varepsilon_{33}$ and, accounting for (44), it takes the form:

$$\begin{aligned} F_{shell}\left(\Delta\varepsilon_q, \zeta^*, \Delta\varepsilon_{33}\right) &= \mathbf{a}\cdot\mathbf{s}_{n+1} - p_{n+1} \\ &= \sqrt{2/3}\, k_{n+1}\left[\cos(\zeta^e - \zeta^*)\, n_{n(33)} + \sin(\zeta^e - \zeta^*)\, m_{n(33)}\right] - p_{n+1} = 0 \end{aligned} \tag{II.2}$$

The internal variables $\left(\Delta\varepsilon_q, \zeta^*, \Delta\varepsilon_{33}\right)$ are computed by solving the system of three equations (46), (47), (II.2) (defined in Table 6 depending on the model branch). This system can be reduced to a 2x2 system since for either model branch, equation (47) can easily be rewritten as an explicit expression $\zeta^*\left(\Delta\varepsilon_q, \Delta\varepsilon_{33}\right)$ and used for eliminating ζ^* from the remaining two equations. This results in a system of nonlinear equations $\hat{F}_1\left(\Delta\varepsilon_q, \Delta\varepsilon_{33}\right) = 0$ and $\hat{F}_{shell}\left(\Delta\varepsilon_q, \Delta\varepsilon_{33}\right) = 0$. More details on the solution of this system are given in Table 8. The above formulation can be easily adjusted to account for plane stress conditions by additionally demanding $\sigma_{13} = \sigma_{23} = 0$, which directly translates to $\Delta\varepsilon_{13} = \Delta\varepsilon_{23} = 0$. Under those conditions, the above algorithm is directly applicable.

For shell elements, the consistent material moduli $D^c_{ep_{\kappa\lambda 33}}$ as developed in section 3 for $\Delta\boldsymbol{\varepsilon}(\Delta\varepsilon_{33})$ can be used, following static condensation to account for constraint (II.1). The condensed material moduli for shell analyses can be calculated as:

Table 8 Integration algorithm for shell element analysis - $\boldsymbol{\sigma_{33} = 0}$

(1) Compute trial elastic stress (elastic prediction)

$$\boldsymbol{\sigma}^e = \boldsymbol{\sigma}_n + \mathbf{D}_{con}\Delta\bar{\boldsymbol{\varepsilon}}, \qquad \mathbf{s}^e = \mathbf{I}^{dev}\boldsymbol{\sigma}^e \ , \qquad p^e = -1/3\,(\mathbf{I}\cdot\boldsymbol{\sigma}^e)$$

$$q^e = \sqrt{3/2}\,\|\mathbf{s}^e\| \ , \qquad k_n = k\left(\varepsilon_{q|n}\right), \qquad F_{n+1}^{trial} = \frac{1}{2G}\left[\|\mathbf{s}^e\| - \sqrt{2/3}\,k_n\right]$$

(2) IF $F_{n+1}^{trial} \le 0$ THEN

$$\Delta\mathbf{e}^p = \mathbf{0} \ , \qquad \Delta\varepsilon_q = 0$$

ELSE ($F_{n+1}^{trial} > 0$)

$$\mathbf{n}_n = \mathbf{s}_n/\|\mathbf{s}_n\|$$

(2a) Assume 1st branch is activated

To find $\Delta\varepsilon_q, \Delta\varepsilon_{33}$ solve the following two equations:

$$\hat{F}_1\left(\Delta\varepsilon_q, \Delta\varepsilon_{33}\right) = F_{p1}\left(\Delta\varepsilon_q, \zeta^*, \Delta\varepsilon_{33}\right) = 0$$

$$\hat{F}_{shell}\left(\Delta\varepsilon_q, \Delta\varepsilon_{33}\right) = F_{shell}\left(\Delta\varepsilon_q, \zeta^*, \Delta\varepsilon_{33}\right) = 0$$

with

$$\tan\zeta^*\left(\Delta\varepsilon_q, \Delta\varepsilon_{33}\right) = \frac{\sin\theta^e}{\frac{\|\mathbf{s}^e\|}{2G\|\Delta\mathbf{e}\|}\left[1 + \frac{h_{n+1}}{3G}\right] - \cos\theta^e}$$

Calculate:

$$\Delta\boldsymbol{\varepsilon} = \Delta\bar{\boldsymbol{\varepsilon}} + \Delta\varepsilon_{33}\mathbf{a}, \qquad \boldsymbol{\sigma}^e = \boldsymbol{\sigma}_n + \mathbf{D}\Delta\boldsymbol{\varepsilon}, \qquad \mathbf{s}^e = \mathbf{I}^{dev}\boldsymbol{\sigma}^e = \mathbf{s}_n + 2G\Delta\mathbf{e}$$

$$\cos\theta^e = \frac{\Delta\mathbf{e}\cdot\mathbf{s}^e}{\|\Delta\mathbf{e}\|\|\mathbf{s}^e\|}, \qquad \bar{h}_{n+1} = h_{n+1}, \qquad \theta = \theta^e + \zeta^*$$

$$\tan\theta^p = \frac{\|\Delta\mathbf{e}\|\sin\theta}{1 + \bar{h}_{n+1}/3G}\Big/\sqrt{3/2}\,\Delta\varepsilon_q$$

(2b) If $\theta^p > \theta_{cr}$: the second branch is activated

To find $\Delta\varepsilon_q, \Delta\varepsilon_{33}$ solve the following two equations:

$$\hat{F}_1\left(\Delta\varepsilon_q, \Delta\varepsilon_{33}\right) = F_{p2}\left(\Delta\varepsilon_q, \zeta^*, \Delta\varepsilon_{33}\right) = 0$$

$$\hat{F}_{shell}\left(\Delta\varepsilon_q, \Delta\varepsilon_{33}\right) = F_{shell}\left(\Delta\varepsilon_q, \zeta^*, \Delta\varepsilon_{33}\right) = 0$$

with

$$\sin\zeta^*\left(\Delta\varepsilon_q, \Delta\varepsilon_{33}\right) = \frac{3G\Delta\varepsilon_q\,\tan\theta_{cr}}{q^e}$$

Calculate:

$$\Delta\boldsymbol{\varepsilon} = \Delta\bar{\boldsymbol{\varepsilon}} + \Delta\varepsilon_{33}\mathbf{a}, \qquad \boldsymbol{\sigma}^e = \boldsymbol{\sigma}_n + \mathbf{D}\Delta\boldsymbol{\varepsilon}, \qquad \mathbf{s}^e = \mathbf{I}^{dev}\boldsymbol{\sigma}^e = \mathbf{s}_n + 2G\Delta\mathbf{e}$$

$$\cos\theta^e = \frac{\Delta\mathbf{e}\cdot\mathbf{s}^e}{\|\Delta\mathbf{e}\|\|\mathbf{s}^e\|}, \quad \theta = \theta^e + \zeta^*$$

$$\bar{h}_{n+1} = 3G\left(\frac{\|\Delta\mathbf{e}\|\sin\theta}{\sqrt{3/2}\,\Delta\varepsilon_q\tan\theta_{cr}} - 1\right)$$

(2c) Calculate the plastic strain increment

$$\mathbf{m}_n = \frac{\left[\mathbf{I}^{dev} - \mathbf{n}_n\otimes\mathbf{n}_n\right]\Delta\mathbf{e}}{\|\left[\mathbf{I}^{dev} - \mathbf{n}_n\otimes\mathbf{n}_n\right]\Delta\mathbf{e}\,\|}, \qquad \cos\zeta^e = \frac{\mathbf{s}_n\cdot\mathbf{s}^e}{\|\mathbf{s}_n\|\|\mathbf{s}^e\|}, \qquad \zeta = \zeta^e - \zeta^*$$

$$\mathbf{n}_{n+1} = \cos\zeta\,\mathbf{n}_n + \sin\zeta\,\mathbf{m}_n, \qquad \mathbf{m}_{n+1} = -\sin\zeta\,\mathbf{n}_n + \cos\zeta\,\mathbf{m}_n$$

$$\Delta\mathbf{e}^p = \sqrt{3/2}\,\Delta\varepsilon_q\,\mathbf{n}_{n+1} + \frac{\|\Delta\mathbf{e}\|\sin\theta}{1 + \bar{h}_{n+1}/3G}\,\mathbf{m}_{n+1}$$

(3) Update stress tensor and state variables:

$$\boldsymbol{\sigma}_{n+1} = \boldsymbol{\sigma}^e - 2G\Delta\mathbf{e}^p$$

Note: *at this stage it should be* $\sigma_{n+1(33)} = 0$

$$\varepsilon_{q|n+1} = \varepsilon_{q|n} + \Delta\varepsilon_q$$

$$D_{ep}^{c,shell}\big|_{\kappa\lambda\mu\nu} = D_{ep}^{c}{}_{\kappa\lambda\mu\nu} - \frac{D_{ep}^{c}{}_{\kappa\lambda 33} D_{ep}^{c}{}_{33\mu\nu}}{D_{ep}^{c}{}_{3333}} \tag{II.3}$$

where $\kappa, \lambda, \mu, \nu = 1,2,3$ but not $\kappa = \lambda = 3$ or $\mu = \nu = 3$. The components $D_{ep}^{c}{}_{\kappa\lambda\mu\nu} \neq D_{ep}^{c}{}_{\mu\nu\kappa\lambda}$ so that the algorithmic moduli for shells are non-symmetric. Expression (II.3) provides the rigidity moduli for plane stress elements for $\kappa, \lambda, \mu, \nu = 1,2$.

II.1 Implementation

For shell element, the extra unknown strain increment component $\Delta\varepsilon_{33}$ needs to be calculated using the additional condition (II.1), to define the plastic corrector. Its derivatives used to solve the 3x3 system are:

$$F_{shell,\Delta\varepsilon_q} = \mathbf{a} \cdot \mathbf{s}_{n+1,\Delta\varepsilon_q} \tag{II.4}$$

$$F_{shell,\zeta^*} = \mathbf{a} \cdot \mathbf{s}_{n+1,\zeta^*} \tag{II.5}$$

$$F_{shell,\Delta\varepsilon_{33}} = \mathbf{a} \cdot \mathbf{s}_{n+1,\Delta\mathbf{e}} - K \tag{II.6}$$

For the two branches of the proposed model, F_2 can be easily rewritten as an explicit expression of angle $\zeta^*\big(\Delta\varepsilon_q, \Delta\mathbf{e}(\Delta\varepsilon_{33})\big)$. This allows for the system to reduce to a single equation of a scalar unknown $\Delta\varepsilon_q$, for three-dimensional elements. Similarly, for shell element implementation, the explicit expression for ζ^* allows for the solution of a simpler system of two unknowns $\big(\Delta\varepsilon_q, \Delta\varepsilon_{33}\big)$, expressed as follows:

$$\hat{F}_1\big(\Delta\varepsilon_q, \Delta\varepsilon_{33}\big) = F_1\big(\Delta\varepsilon_q, \zeta^*\big(\Delta\varepsilon_q, \Delta\varepsilon_{33}\big), \Delta\varepsilon_{33}\big) = 0 \tag{II.7}$$

$$\hat{F}_{shell}\big(\Delta\varepsilon_q, \Delta\varepsilon_{33}\big) = F_{shell}\big(\Delta\varepsilon_q, \zeta^*\big(\Delta\varepsilon_q, \Delta\varepsilon_{33}\big), \Delta\varepsilon_{33}\big) = 0 \tag{II.8}$$

To solve the system of equations (II.7) and (II.8), a local Newton scheme is used; assuming from some trial values $\big(\Delta\varepsilon_q, \Delta\varepsilon_{33}\big)$, functions $\hat{F}_1$, $\hat{F}_{shell}$ and their derivatives are calculated. A correction to these trial values $\Big(\delta\big(\Delta\varepsilon_q\big), \delta\big(\Delta\varepsilon_{33}\big)\Big)$ is obtained as follows:

$$\begin{bmatrix} A_{11} & A_{12} \\ A_{21} & A_{22} \end{bmatrix} \cdot \begin{bmatrix} \delta(\Delta\varepsilon_q) \\ \delta(\Delta\varepsilon_{33}) \end{bmatrix} = \begin{bmatrix} b_1 \\ b_2 \end{bmatrix} \tag{II.9}$$

or

$$\begin{bmatrix} \delta(\Delta\varepsilon_q) \\ \delta(\Delta\varepsilon_{33}) \end{bmatrix} = \frac{1}{A_{11}A_{22} - A_{12}A_{21}} \begin{bmatrix} A_{22} & -A_{12} \\ -A_{21} & A_{11} \end{bmatrix} \cdot \begin{bmatrix} b_1 \\ b_2 \end{bmatrix} \tag{II.10}$$

In the above equations, A_{ij} and b_i are obtained by the following expressions:

$$A_{11} = \frac{\partial \hat{F}_1}{\partial \Delta\varepsilon_q} = F_{1,\Delta\varepsilon_q} + F_{1,\zeta^*}\zeta^*_{,\Delta\varepsilon_q} \tag{II.11}$$

$$A_{12} = \frac{\partial \hat{F}_1}{\partial \Delta\varepsilon_{33}} = \mathbf{a} \cdot \left[F_{1,\Delta\mathbf{e}} + F_{1,\zeta^*}\zeta^*_{,\Delta\mathbf{e}}\right] \tag{II.12}$$

$$A_{21} = \frac{\partial \hat{F}_{shell}}{\partial \Delta\varepsilon_q} = \mathbf{a} \cdot \left[\mathbf{s}_{n+1,\Delta\varepsilon_q} + \mathbf{s}_{n+1,\zeta^*}\zeta^*_{,\Delta\varepsilon_q}\right] \tag{II.13}$$

$$A_{22} = \frac{\partial \hat{F}_{shell}}{\partial \Delta\varepsilon_{33}} = \mathbf{a} \cdot \left[\mathbf{a} \cdot \mathbf{s}_{n+1,\Delta\mathbf{e}} + \mathbf{a} \cdot \mathbf{s}_{n+1,\zeta^*}\zeta^*_{,\Delta\mathbf{e}}\right] - K \tag{II.14}$$

and

$$b_1 = -\hat{F}_1\left(\Delta\varepsilon_q, \Delta\varepsilon_{33}\right) = -F_1\left(\Delta\varepsilon_q, \zeta^*\left(\Delta\varepsilon_q, \Delta\varepsilon_{33}\right), \Delta\varepsilon_{33}\right) \tag{II.15}$$

$$b_2 = -\hat{F}_{shell}\left(\Delta\varepsilon_q, \Delta\varepsilon_{33}\right) = -F_{shell}\left(\Delta\varepsilon_q, \zeta^*\left(\Delta\varepsilon_q, \Delta\varepsilon_{33}\right), \Delta\varepsilon_{33}\right) \tag{II.16}$$

The derivatives $\zeta^*_{,\Delta\varepsilon_q}$, $\zeta^*_{,\Delta\mathbf{e}}$ can be calculated by differentiating $\zeta^*\left(\Delta\varepsilon_q, \Delta\mathbf{e}(\Delta\varepsilon_{33})\right)$, or equivalently, directly from F_2:

$$\zeta^*_{,\Delta\varepsilon_q} = -F_{2,\Delta\varepsilon_q} \,/\, F_{2,\zeta^*} \tag{II.17}$$

$$\zeta^*_{,\Delta\mathbf{e}} = -\,F_{2,\Delta e}/F_{2,\zeta^*} \tag{II.18}$$

Derivatives $\mathbf{s}_{n+1,\Delta\varepsilon_q}, \mathbf{s}_{n+1,\zeta^*}, \mathbf{s}_{n+1,\Delta\mathbf{e}}, F_{1,\Delta\varepsilon_q}, F_{1,\zeta^*}, F_{1,\Delta\mathbf{e}}, F_{1,\zeta^*}, F_{2,\Delta\varepsilon_q}, F_{2,\zeta^*}, F_{2,\Delta e}$ have been presented earlier in this Appendix, and are summed up in Table 9. The trial values of $\Delta\varepsilon_q$ and $\Delta\varepsilon_{33}$ are updated as in (II.19) and the iterative process continues until both b_1 and b_2 vanish, as indicated in Table 9.

$$\begin{aligned} \Delta\varepsilon_q &\leftarrow \Delta\varepsilon_q + \delta\left(\Delta\varepsilon_q\right) \\ \Delta\varepsilon_{33} &\leftarrow \Delta\varepsilon_{33} + \delta(\Delta\varepsilon_{33}) \end{aligned} \tag{II.19}$$

Table 9 Newton scheme for solving the system of $\widehat{\boldsymbol{F}}_{\boldsymbol{1}}$ and $\widehat{\boldsymbol{F}}_{\boldsymbol{shell}}$ for shell elements

	$\mathbf{n}_n = \mathbf{s}_n/\|\mathbf{s}_n\|, \quad k_n = k(\varepsilon_{q\|n})$ $\Delta\varepsilon_q = 0, \quad \delta(\Delta\varepsilon_q) = 0\,, \hat{F}_1 = 1E+032$ $\Delta\varepsilon_{33} = 0,\ \delta(\Delta\varepsilon_{33}) = 0, \hat{F}_{shell} = 1E+032$
WHILE	$\max\{\|\hat{F}_1\|, \|\hat{F}_{shell}\|\} > TOL$
	$\Delta\varepsilon_q = \Delta\varepsilon_q + \delta(\Delta\varepsilon_q), \quad \Delta\varepsilon_{33} = \Delta\varepsilon_{33} + \delta(\Delta\varepsilon_{33})$
	$\Delta\boldsymbol{\varepsilon} = \Delta\bar{\boldsymbol{\varepsilon}} + \Delta\varepsilon_{33}\mathbf{a}$ $\boldsymbol{\sigma}^e = \boldsymbol{\sigma}_n + \mathbf{D}\Delta\boldsymbol{\varepsilon} \quad , \quad \mathbf{s}^e = \mathbf{I}^{dev}\boldsymbol{\sigma}^e = \mathbf{s}_n + 2G\Delta\mathbf{e}$ $p^e = -1/3\,(\mathbf{I}\cdot\boldsymbol{\sigma}^e)\,, \quad q^e = \sqrt{3/2}\,\|\mathbf{s}^e\|$
	$\mathbf{m}_n = \dfrac{[\mathbf{I}^{dev} - \mathbf{n}_n \otimes \mathbf{n}_n]\,\Delta\mathbf{e}}{\|[\mathbf{I}^{dev} - \mathbf{n}_n \otimes \mathbf{n}_n]\,\Delta\mathbf{e}\,\|}, \quad \mathbf{m}_{n,\Delta\mathbf{e}}(\mathrm{I}.6)$ $\cos\zeta^e = \mathbf{s}_n\cdot\mathbf{s}^e/\|\mathbf{s}_n\|\|\mathbf{s}^e\|\,, \quad \zeta^e_{,\Delta\mathbf{e}}(\mathrm{I}.5)$ $\cos\theta^e = \Delta\mathbf{e}\cdot\mathbf{s}^e/\|\Delta\mathbf{e}\|\|\mathbf{s}^e\|\,, \quad \theta^e_{,\Delta\mathbf{e}}(\mathrm{I}.7)$ $\cos\theta_n = \mathbf{s}_n\cdot\Delta\mathbf{e}/\|\mathbf{s}_n\|\|\Delta\mathbf{e}\|$
	1st branch — 2nd branch
ζ^*	$\tan\zeta^* = \dfrac{\sin\theta^e}{\frac{\|\mathbf{s}^e\|}{2G\|\Delta\mathbf{e}\|}\left[1+\frac{h_{n+1}}{3G}\right] - \cos\theta^e}$ — $\sin\zeta^* = \dfrac{3G\Delta\varepsilon_q\,\tan\theta_{cr}}{q^e}$
	$\theta = \theta^e + \zeta^*$ $\zeta = \zeta^e - \zeta^*$ $\mathbf{n}_{n+1} = \cos\zeta\,\mathbf{n}_n + \sin\zeta\,\mathbf{m}_n$ $\mathbf{m}_{n+1} = -\sin\zeta\,\mathbf{n}_n + \cos\zeta\,\mathbf{m}_n$ $\mathbf{s}_{n+1} = \sqrt{2/3}\,k_{n+1}\,\mathbf{n}_{n+1}(\mathrm{I}.1)$ $\mathbf{s}_{n+1,\Delta\varepsilon_q}(\mathrm{I}.2), \quad \mathbf{s}_{n+1,\zeta^*}(\mathrm{I}.3), \quad \mathbf{s}_{n+1,\Delta\mathbf{e}}(\mathrm{I}.4)$
	1st branch — 2nd branch
F_1 & F_2	(I.8) & (I.9) — (I.21) & (I.22)
$F_{1,\Delta\varepsilon_q}$ & $F_{2,\Delta\varepsilon_q}$	(I.11) & (I.14) — (I.23) & (I.26)
F_{1,ζ^*} & F_{2,ζ^*}	(I.12) & (I.15) — (I.24) & (I.27)
$F_{1,\Delta\mathbf{e}}$ & $F_{2\,\Delta\mathbf{e}}$	(I.13) & (I.16) — (I.25) & (I.28)
	$\hat{F}_1 = F_1(\Delta\varepsilon_q, \zeta^*, \Delta\varepsilon_{33})$ $\hat{F}_{shell} = F_{shell}(\Delta\varepsilon_q, \zeta^*, \Delta\varepsilon_{33})$(I.38) Calculate $A_{11}, A_{12}, A_{21}, A_{22}$ and the corrections $\delta(\Delta\varepsilon_q), \delta(\Delta\varepsilon_{33})$ $A_{11} = F_{1,\Delta\varepsilon_q} + F_{1,\zeta^*}\zeta^*_{,\Delta\varepsilon_q} \quad , \ A_{12} = \mathbf{a}\cdot\left[F_{1,\Delta\mathbf{e}} + F_{1,\zeta^*}\zeta^*_{,\Delta\mathbf{e}}\right]$ $A_{21} = \mathbf{a}\cdot\left[\mathbf{s}_{n+1,\Delta\varepsilon_q} + \mathbf{s}_{n+1,\zeta^*}\zeta^*_{,\Delta\varepsilon_q}\right], \ A_{22} = \mathbf{a}\cdot\left[\mathbf{a}\cdot\mathbf{s}_{n+1,\Delta\mathbf{e}} + \mathbf{a}\cdot\mathbf{s}_{n+1,\zeta^*}\zeta^*_{,\Delta\mathbf{e}}\right] - K$ where $\zeta^*_{,\Delta\varepsilon_q} = -F_{2,\Delta\varepsilon_q}/F_{2,\zeta^*}, \ \zeta^*_{,\Delta\mathbf{e}} = -F_{2,\Delta e}/F_{2,\zeta^*}$ $\begin{bmatrix}\delta(\Delta\varepsilon_q)\\ \delta(\Delta\varepsilon_{33})\end{bmatrix} = \dfrac{1}{A_{11}A_{22} - A_{12}A_{21}}\begin{bmatrix}A_{22} & -A_{12}\\ -A_{21} & A_{11}\end{bmatrix}\cdot\begin{bmatrix}-\hat{F}_1\\ -\hat{F}_{shell}\end{bmatrix}$
END	

References

Bardi, F. C., & Kyriakides, S. (2006). Plastic buckling of circular tubes under axial compression-part I: Experiments. International Journal of Mechanical Sciences, 48(8), 830–841. https://doi.org/10.1016/j.ijmecsci.2006.03.005

Bardi, F. C., Kyriakides, S., & Yun, H. D. (2006). Plastic buckling of circular tubes under axial compression-part II: Analysis. International Journal of Mechanical Sciences, 48(8), 842–854. https://doi.org/10.1016/j.ijmecsci.2006.03.002

Batdorf, S. B. (1949). Theories of Plastic Buckling. Journal of the Aeronautical Sciences, 16(7), 405–408. https://doi.org/10.2514/8.11821

Batterman, S. C. (1965). Plastic buckling of axially compressed circular cylindrical shells. AIAA Journal, 3(2), 316–325. https://doi.org/10.2514/3.2848

Budiansky, B. (1959). A reassessment of deformation theories for plasticity. Journal of Applied Mechanics, 26, 259–264.

Blachut, J., Galletly, G. D., & James, S. (1996). On the Plastic Buckling Paradox for Cylindrical Shells. Proceedings of the Institution of Mechanical Engineers, Part C: Journal of Mechanical Engineering Science, 210(5), 477–488. https://doi.org/10.1243/PIME_PROC_1996_210_221_02

Bushnell, D. (1974). Bifurcation buckling of shells of revolution including large deflections, plasticity and creep. International Journal of Solids and Structures, 10(11), 1287–1305. https://doi.org/10.1016/0020-7683(74)90073-0

Chakrabarty, J. (2006). Theory of Plasticity (3rd ed.). https://doi.org/10.1016/C2009-0-05774-2

Christoffersen, J., & Hutchinson, J. W. (1979). A class of phenomenological corner theories of plasticity. Journal of the Mechanics and Physics of Solids, 27(5–6), 465–487.

https://doi.org/10.1016/0022-5096(79)90026-7

Corona, E., Lee, L. H., & Kyriakides, S. (2006). Yield anisotropy effects on buckling of circular tubes under bending. International Journal of Solids and Structures, 43(22–23), 7099–7118. https://doi.org/10.1016/j.ijsolstr.2006.03.005

Gellin, S. (1979). Effect of an axisymmetric imperfection on the plastic buckling of an axially compressed cylindrical shell. Journal of Applied Mechanics, Transactions ASME, 46(1), 125–131. https://doi.org/10.1115/1.3424483

Gerard, G., & Becker, H. (1957). Handbook of Structural Stability – Part III – Buckling of Curved Plates and Shells. National advisory committee for aeronautics.

Giezen, J. J. (1988). Plastic buckling of cylinders under biaxial loading, PhD Thesis. California Institute of Technology.

Gotoh, M. (1985). A Simple Plastic Constitutive Equation with Vertex Effect. Engineering Fracture Mechanics, 21(4), 673–684. https://doi.org/0013-7644/85

Goya, M., & Ito, K. (1991). An expression of elastic-plastic constitutive law incorporating vertex formation and kinematic hardening. Trans. ASME: J. Appl. Mech., 58(September 1991), 617–622. https://doi.org/10.1115/1.2897240.

Hecker, S. S. (1972). Experimental investigation of corners in the yield surface. Acta Mechanica, 13(1–2), 69–86. https://doi.org/10.1007/BF01179659

Hughes, T. J. R., & Shakib, F. (1986). Psedo-corner theory: A simple enhancement of J_2 flow theory for applications involving non-proportional loading. Engineering Computations, 3(2), 116–120. https://doi.org/https://doi.org/10.1108/eb023649 Permanent

Hutchinson, J. W. (1974). Plastic Buckling. Advances in Applied Mechanics, Vol. 14, pp. 67–144. https://doi.org/10.1016/S0065-2156(08)70031-0

Hutchinson, J. W., & Budiansky, B. (1976). Analytical and Numerical Study of the Effects of Initial Imperfections on the Inelastic Buckling of a Cruciform Column. In B. Budiansky (Ed.), Buckling of Structures (pp. 98–105). Berlin, Heidelberg: Springer Berlin Heidelberg.

Ju, G. T., & Kyriakides, S. (1991). Bifurcation Buckling Versus Limit Load Instabilities of Elastic-Plastic Tubes Under Bending and External Pressure. Journal of Offshore Mechanics and Arctic Engineering, 113(1), 43. https://doi.org/10.1115/1.2919895

Ju, G. T., & Kyriakides, S. (1992). Bifurcation and localization instabilities in cylindrical shells under bending-II. Predictions. International Journal of Solids and Structures, 29(9), 1143–1171. https://doi.org/10.1016/0020-7683(92)90140-O

Kuroda, M., & Tvergaard, V. (1999). Use of abrupt strain path change for determining subsequent yield surface: illustrations of basic idea. Acta Materialia, 47(14), 3879–3890. https://doi.org/10.1016/S1359-6454(99)00213-X

Kuroda, M., & Tvergaard, V. (2001). A phenomenological plasticity model with non-normality effects representing observations in crystal plasticity. Journal of the Mechanics and Physics of Solids, 49(6), 1239–1263. https://doi.org/10.1016/S0022-5096(00)00080-6

Kuwabara, T., Kuroda, M., Tvergaard, V., & Nomura, K. (2000). Use of abrupt strain path change for determining subsequent yield surface: experimental study with metal sheets. Acta Materialia, 48, 2071–2079. https://doi.org/10.1016/S1359-6454(00)00048-3

Kyriakides, S., Bardi, F. C., & Paquette, J. A. (2005). Wrinkling of circular tubes under axial compression: Effect of anisotropy. Journal of Applied Mechanics, Transactions ASME, 72(2), 301–305. https://doi.org/10.1115/1.1839590

Kyriakides, S., & Corona, E. (2007). Mechanics of Offshore Pipelines: Volume 1 Buckling and Collapse (1st ed., p. 448). 1st ed., p. 448. https://doi.org/10.1128/JCM.03067-14

Lee, L. H. N. (1962). Inelastic Buckling of Initially Imperfect Cylindrical Shells Subject to Axial Compression. Journal of the Aerospace Sciences, 29(1), 87–95. https://doi.org/10.2514/8.9306

Needleman, A., & Tvergaard, V. (1982). Aspects of Plastic Postbuckling Behavior. In Mechanics of Solids (pp. 453–498). https://doi.org/10.1016/B978-0-08-025443-2.50020-3

Pappa, P., & Karamanos, S. A. (2016). Non-associative J_2 plasticity model for finite element buckling analysis of shells in the inelastic range. Computer Methods in Applied Mechanics and Engineering, 300, 689–715. https://doi.org/10.1016/j.cma.2015.11.031

Peek, R. (2000). An incrementally continuous deformation theory of plasticity with unloading. International Journal of Solids and Structures, 37(36), 5009–5032. https://doi.org/10.1016/S0020-7683(99)00294-2

Peek, R., & Hilberink, A. (2013). Axisymmetric wrinkling of snug-fit lined pipe. International Journal of Solids and Structures, 50(7–8), 1067–1077. https://doi.org/10.1016/j.ijsolstr.2012.11.023

Rønning, L., Hopperstad, O. S., & Larsen, P. K. (2010). Numerical study of the effects of constitutive models on plastic buckling of plate elements. European Journal of Mechanics - A/Solids, 29(4), 508–522. https://doi.org/10.1016/j.euromechsol.2010.02.001

Schurig, M. (2006). The Vertex Effect in Polycrystalline Materials, PhD Thesis (Otto- von-Guericke-Universität Magdeburg). Retrieved from http://diglib.uni-magdeburg.de/Dissertationen/2006/micschurig.htm

Shamass, R., Alfano, G., & Guarracino, F. (2014). A numerical investigation into the plastic buckling paradox for circular cylindrical shells under axial compression. Engineering Structures, 75, 429–447. https://doi.org/10.1016/j.engstruct.2014.05.050

Simo, J. C. (1987). A J_2-flow theory exhibiting a corner-like effect and suitable for large-scale computation. Computer Methods in Applied Mechanics and Engineering, 62(2), 169–194.

https://doi.org/10.1016/0045-7825(87)90022-3

Simo, J. C., & Taylor, R. L. (1985). Consistent tangent operators for rate-independent elastoplasticity. Computer Methods in Applied Mechanics and Engineering, 48(1), 101–118. https://doi.org/10.1016/0045-7825(85)90070-2

Tuğcu, P. (1991). Plate buckling in the plastic range. International Journal of Mechanical Sciences, 33(1), 1–11. https://doi.org/10.1016/0020-7403(91)90023-V

Tvergaard, V. (1983a). On the transition from a diamond mode to an axisymmetric mode of collapse in cylindrical shells. International Journal of Solids and Structures, 19(10), 845–856. https://doi.org/10.1016/0020-7683(83)90041-0

Tvergaard, V. (1983b). Plastic buckling of axially compressed circular cylindrical shells. Thin-Walled Structures, 1(2), 139–163. https://doi.org/10.1016/0263-8231(83)90018-6

Tvergaard, V., & Needleman, A. (2000). Buckling localization in a cylindrical panel under axial compression. International Journal of Solids and Structures, 37(46), 6825–6842. https://doi.org/10.1016/S0020-7683(99)00316-9

Wang, C. M., Xiang, Y., & Chakrabarty, J. (2001). Elastic / plastic buckling of thick plates. International Journal of Solids and Structures, 38, 8617–8640. https://doi.org/10.1016/S0020-7683(01)00144-5

Yoshida, K. (2017). A plastic flow rule representing corner effects predicted by rate-independent crystal plasticity. International Journal of Solids and Structures, 120(May 2017), 1339–1351. https://doi.org/10.1016/j.ijsolstr.2017.05.004

Yoshida, K., & Tsuchimoto, T. (2018). Plastic flow of thin-walled tubes under nonlinear tension-torsion loading paths and an improved pseudo-corner model. International Journal of Plasticity, 104(February), 214–229. https://doi.org/10.1016/j.ijplas.2018.02.013